Geodetic displacements and aftershocks following the 2001 M_w = 8.4 Peru earthquake: Implications for the mechanics of the earthquake cycle along subduction zones

H. Perfettini
Institut de Recherche pour le Développement, Laboratoire des Mécanismes de Transferts en Géologie, Toulouse, France

J.-P. Avouac
Tectonics Observatory, California Institute of Technology, Pasadena, California, USA

J.-C. Ruegg
Institut de Physique du Globe de Paris, Paris, France

Received 4 November 2004; revised 6 May 2005; accepted 2 June 2005; published 3 September 2005.

[1] We analyzed aftershocks and postseismic deformation recorded by the continuous GPS station AREQ following the M_w = 8.4, 23 June 2001 Peru earthquake. This station moved by 50 cm trenchward, in a N235°E direction during the coseismic phase, and continued to move in the same direction for an additional 15 cm over the next 2 years. We compare observations with the prediction of a simple one-dimensional (1-D) system of springs, sliders, and dashpot loaded by a constant force, meant to simulate stress transfer during the seismic cycle. The model incorporates a seismogenic fault zone, obeying rate-weakening friction, a zone of deep afterslip, the brittle creep fault zone (BCFZ) obeying rate-strengthening friction, and a zone of viscous flow at depth, the ductile fault zone (DFZ). This simple model captures the main features of the temporal evolution of seismicity and deformation. Our results imply that crustal strain associated with stress accumulation during the interseismic period is probably not stationary over most of the interseismic period. The BCFZ appears to control the early postseismic response (afterslip and aftershocks), although an immediate increase, by a factor of about 1.77, of ductile shear rate is required, placing constraints on the effective viscosity of the DFZ. Following a large subduction earthquake, displacement of inland sites is trenchward in the early phase of the seismic cycle and reverse to landward after a time t_i for which an analytical expression is given. This study adds support to the view that the decay rate of aftershocks may be controlled by reloading due to deep afterslip. Given the ratio of preseismic to postseismic viscous creep, we deduce that frictional stresses along the subduction interface account for probably 70% of the force transmitted along the plate interface.

Citation: Perfettini, H., J.-P. Avouac, and J.-C. Ruegg (2005), Geodetic displacements and aftershocks following the 2001 M_w = 8.4 Peru earthquake: Implications for the mechanics of the earthquake cycle along subduction zones, *J. Geophys. Res.*, *110*, B09404, doi:10.1029/2004JB003522.

1. Introduction

[2] Large earthquakes are followed by a phase of postseismic relaxation during which the fault zone and the surrounding medium deform in response to the stress variations induced by the coseismic stress drop. Aftershocks and geodetic strain are obvious manifestations of this relaxation phase but the physical mechanisms governing these effects remain unclear. Our understanding of these processes should benefit greatly from the development of geodetic monitoring from continuous GPS stations, in particular because it becomes possible to analyze jointly the temporal evolution of seismicity and of surface strain. Here we focus on postseismic effects following the 23 June 2001 M_w = 8.4 Peru (or Arequipa) earthquake, which is the largest earthquake recorded along the subduction interface between the Nazca and South American plates (see Figure 1) since the 1960 great Chile (M_w = 9.5) earthquake. The time evolution of the deformation was recorded at one of the stations from the network of permanent stations from International GPS Service (GPS) [*Zumberge et al.*, 1995]. In addition to being of exceptionally high magnitude this particular earthquake is thus one of the few examples for which a good record of postseismic geodetic displacement is available [*Ruegg et al.*, 2001; *Melbourne and Webb*, 2002].

[3] Hereafter we first recall possible mechanisms driving postseismic relaxation and aftershocks. We next describe the M_w = 8.4, 23 June 2001 Peru earthquake and the GPS record

0148-0227/05/2004JB003522$09.00

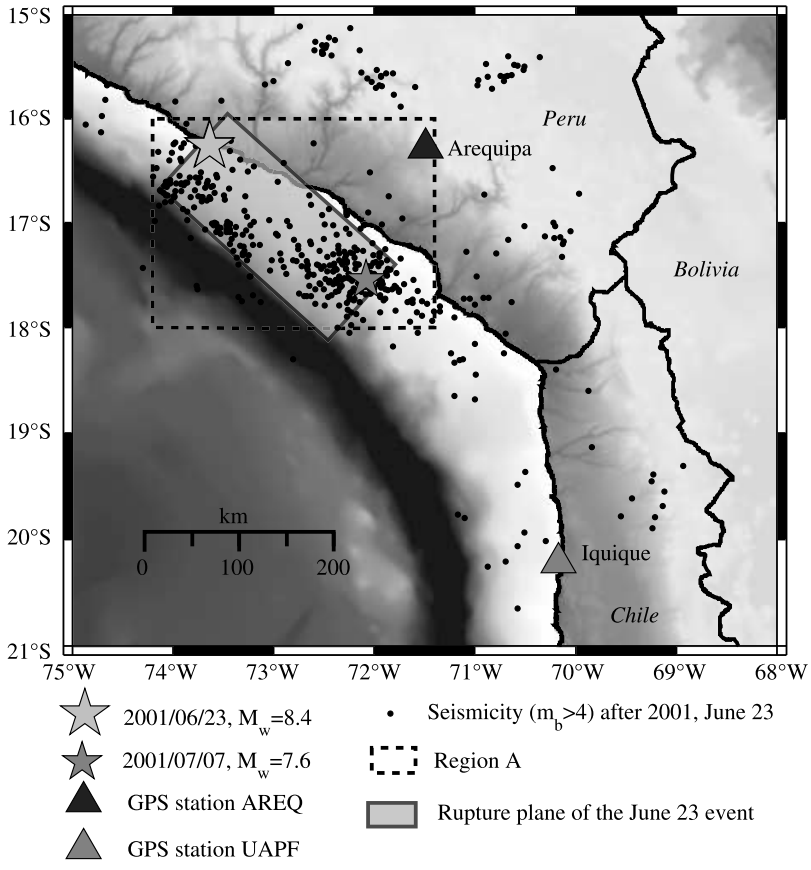

Figure 1. Seismicity ($m_b > 4$) after (black circles) the $M_w = 8.4$, 23 June 2001, south Peru earthquake (light gray star). Data come from the NEIC catalog. The approximate rupture plane is displayed by the gray opaque rectangle. The 7 July aftershock of $M_w = 7.6$ (dark gray star) occurs at the southern end of the rupture plane of the main shock. The two GPS stations used in this study are AREQ (black triangle, city of Arequipa) and UAPF (gray triangle, city of Iquique). The area where seismicity is considered (dashed rectangle or region A) covers most of the aftershocks.

of postseismic relaxation. We then show that the observed geodetic records can be well explained from a simple model combining afterslip, obeying rate-strengthening fiction and viscous flow, and that postseismic reloading resulting from this relaxation probably controls the time evolution of the aftershock sequence. [*Perfettini and Avouac*, 2004a] showed, by comparing seismicity and geodetic measures following the $M_w = 7.6$ Chi-Chi earthquake that the temporal evolution of aftershocks was governed by reloading due to the relaxation of the brittle creep fault zone (BCFZ). We will show here that the same relation seems to hold in the case of the 2001 Arequipa subduction earthquake.

2. Postseismic Relaxation Processes

2.1. Postseismic Strain

[4] Geodetic measurements of postseismic relaxation are generally interpreted to result from a combination of afterslip on the ruptured fault plane, or on unruptured fault patches near the surface (shallow afterslip) or downdip of the ruptured area (deep afterslip), and viscous deformation of the lower crust and upper mantle [e.g., *Brown et al.*, 1977; *Marone et al.*, 1991; *Pollitz et al.*, 1998; *Segall et al.*, 1995; *Cohen*, 1999; *Freymueller et al.*, 2000; *Pollitz et al.*, 2000; *Wang et al.*, 2001; *Melbourne et al.*, 2002; *Hearn et al.*, 2002; *Burgmann et al.*, 2002; *Márquez-Azúa et al.*, 2002; *Hsu et al.*, 2002; *Miyazaki et al.*, 2004; *Chlieh et al.*, 2004]. The respective contributions of each of these processes are poorly known however, and they probably vary depending on the local tectonic context. [*Montési*, 2004] has analyzed a number of examples of GPS records of postseismic relaxation from a simple one-dimensional (1-D) model of fault rheology and found that depending on the case, the time evolution of deformation was dominantly governed by brittle afterslip or viscous relaxation. This analysis had limited success probably because it was ignoring reloading due to interseismic strain and coupling between brittle creep and viscous deformation.

[5] Deep afterslip seems a dominant factor in the early phase of relaxation, up to about 1 year or so, and is located immediately below the area that ruptured during the main shock. The most compelling evidence that afterslip occurs predominantly in the transition zone where interseismic slip tapers from zero to the interplate slip rate probably comes from the comparison of interferometric synthetic aperture radar measurements of interseismic, coseismic and postseismic deformation along the Chile subduction zone where the $M_w = 8.1$ Antofagasta earthquake occurred [*Chlieh et al.*, 2004]. If afterslip is governed by rate-strengthening brittle deformation, it should approximately follow a loga-

rithmic time evolution, equivalent to a $1/t$ decay of slip rate [e.g., *Marone et al.*, 1991; *Hearn et al.*, 2002; *Perfettini and Avouac*, 2004a]. Evidence for a $1/t$ varying afterslip was found from the analysis of postseismic deformation following in particular the M_w = 9.2, 1964 Alaska earthquake [*Cohen*, 1998], the M_w = 7.4, 1999 Izmit earthquake [*Hearn et al.*, 2002], the M_w = 8.0 Colima-Jalisco earthquake [*Hutton et al.*, 2001] and the M_w = 7.6 Chi-Chi earthquake [*Perfettini and Avouac*, 2004a]. These examples show that this mechanism probably plays a major role in postseismic relaxation whatever the particular tectonic context since the Izmit earthquake occurred on a strike-slip fault, the Chi-Chi earthquake occurred on an intracontinental thrust fault, while the 1964 Alaska and the Colima-Jalisco earthquakes are major subduction events.

[6] Viscous relaxation occurs presumably at greater depth, where ductile processes become dominant over brittle processes due to pressure and temperature increase [e.g., *Cohen*, 1999; *Wang et al.*, 2001]. The characteristic relaxation time associated with viscous relaxation is estimated to be much larger than that associated with afterslip, being probably of the order of a few centuries to a few thousand years. Unambiguous examples of viscous postseismic relaxation are scarce. They include postseismic deformation following the great M_w = 9.5, 1960 Chile and the M_w = 9.2, 1964 Alaska earthquakes [*Freymueller et al.*, 2000; *Khazaradze et al.*, 2002]. In both cases, geodetic measurements made several decades after the main shock revealed that sites some hundreds of kilometers away from the trench were moving trenchward, in the opposite direction expected from interseismic strain, a pattern consistent with the predictions of mechanical models of viscous relaxation [e.g., *Wang et al.*, 2001].

2.2. Possible Mechanisms Driving Aftershocks

[7] The current view is that the spatial distribution of aftershocks result from the redistribution of stress during the coseismic phase [e.g., *King et al.*, 1994]. The mechanism explaining the seismicity rate change is more enigmatic. Some authors have proposed that it may be controlled by (1) pore pressure variations [*Nur and Booker*, 1972; *Bosl and Nur*, 2002], (2) reloading of the brittle crust as a result of postseismic viscous flow [*Deng et al.*, 1999], (3) reloading of the brittle crust by postseismic afterslip [*Perfettini and Avouac*, 2004a], or (4) the response to the coseismic stress variation of a population of noninteracting faults obeying rate-weakening rate and state friction [*Dieterich*, 1994]. Mechanisms 2 and 3 are testable in a straightforward manner by comparing geodetic records with seismicity.

[8] *Deng et al.* [1999] found that stress loading driven by viscous relaxation could explain the decay rate of aftershocks following the 1994 Northridge earthquake but the fit was poor during the first 8 months of postseismic relaxation, a period during which most of the aftershocks are produced. In the early phase, seismicity rate decayed much more rapidly than predicted from their model. Also, there was no geodetic time series so that the time evolution of crustal strain was largely unconstrained. Thus it is not possible for this particular case to really assess the similarity of time evolution of crustal strain and seismicity.

[9] *Perfettini and Avouac* [2004a] have suggested that deep afterslip should be more effective in producing stress variations in the upper brittle crust. They showed that the time evolution of afterslip following the Chi-Chi earthquake [*Hsu et al.*, 2002] was consistent with the observed decay rate of aftershocks. This analysis took into account reloading by interseismic strain but ignored viscous relaxation. Hereafter we use a refined formulation which accounts for potential acceleration of ductile flow and its effect on deep afterslip [*Perfettini and Avouac*, 2004b], a refinement that seems necessary to reproduce the postseismic displacements observed following the Peru earthquake. We believe that the formulation presented here applies to any tectonic setting.

3. The M_w = 8.4, 23 June 2001 Peru Earthquake

[10] The M_w = 8.4, 23 June 2001 Peru (or Arequipa) earthquake occurred along the coast of Peru at the boundary between the Nazca and South American plates (see Figure 1). At this place the two plates are converging by about 79 mm/yr, in a N55°E direction as indicated from global plate models [*DeMets et al.*, 1990; *Sella et al.*, 2002]. A fraction of the convergence rate is absorbed by crustal shortening across the Andes [*Hindle et al.*, 2002]. Although not very well constrained, this term is estimated to be less than 10 mm/yr, a reasonable value being probably around 5 mm/yr at this latitude [e.g., *Lamb*, 2000], the remaining fraction being taken up by slip along the subduction interface. The return period of large subduction events in this area is estimated to about 120 years [*Dorbath et al.*, 1990].

[11] Seismological inversions suggest that the rupture broke an area of the order of 200 × 100 km^2 with a mean slip of 2.8 m and a stress drop of 1.9 MPa [*Kikuchi and Yamanaka*, 2001]. *Bilek and Ruff* [2002] proposed that the dimension of rupture is 300 × 100 km on the basis of the aftershock distribution or 180 × 100 km with an average slip ranging from 5 to 8.4 m, on the basis of the analysis of broadband seismic waveforms. Using an inversion of the GPS coseismic displacements, J.-C. Ruegg et al. (unpublished manuscript, 2002) found a rupture dimension of 300 × 150 km^2 and a mean slip of about 2 m. Therefore the dimension of the downdip extent of the ruptured fault area must be about 100–150 km. Coseismic and postseismic deformations were recorded by the IGS continuous GPS station at Arequipa (AREQ). Previous investigations have shown that relative to South America, AREQ moved by about 44 cm in a N55°E direction during the coseismic phase [*Ruegg et al.*, 2001; *Melbourne and Webb*, 2002].

3.1. Description of the GPS Data and Processing Strategy

[12] The GPS observations collected over the period 2000.0 to 2003.5 at AREQ were analyzed together with the GPS data of seven other IGS permanent stations in South America (CORD, EISL, FORT, KOUR, LPGS, OHIG and SANT), and the data of the GPS station UAPF at Iquique (Chile). The UAPF (Arturo Prat University) GPS station has been continuously operating since 1995 as part of a French-Chilean project for study of the seismic cycle [*Ruegg et al.*, 2001]. It is located 442 km south of Arequipa and 570 km south east of the main shock epicenter. The data

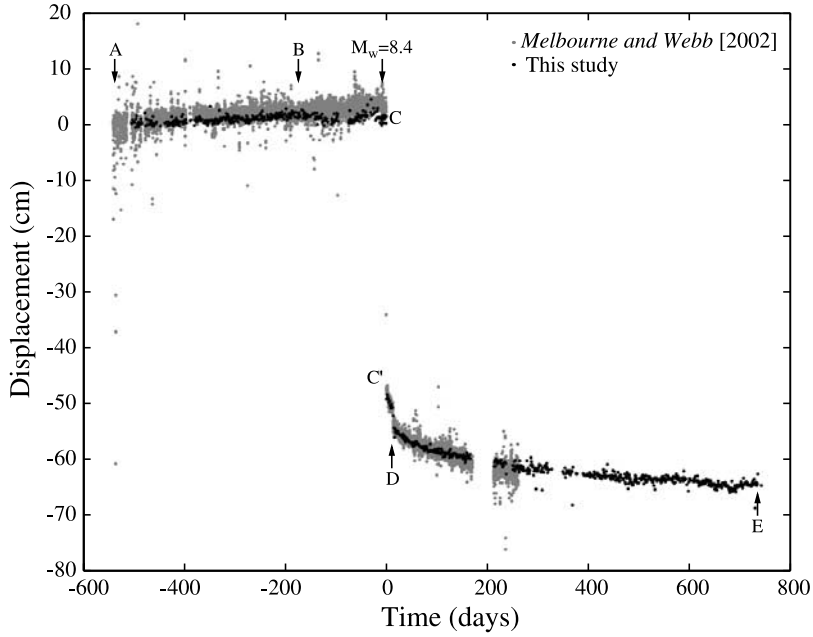

Figure 2. Displacement in the N55° direction at GPS station AREQ relative to South America in a period covering the 2001 M_w = 8.4 south Peru event. The gray dots represent the processing of *Melbourne and Webb* [2002] using only AREQ, while the black dots represent our processing obtained considering both AREQ and UAPF.

are processed using the GAMIT software [*King and Bock*, 1998] to obtain daily independent solutions. In each daily solution we calculated, for each available station, the coordinates and associated parameters (tropospheric zenital delay and phase ambiguity) using doubly differenced GPS phase measurements. We use IGS precise orbits and IERS Earth orientation parameters given by the Scripps Orbit and Permanent Array Center (http://sopac.ucsd.edu). The coordinates of the IGS stations located on the cratonic part of the South American plate (KOUR, FORT, LPGS and CORD), where constrained to their values and uncertainties in the International Terrestrial Reference Frame (ITRF2000, [*Altamimi et al.*, 2002]) at the date of each daily solution. The a priori coordinates of other stations (and in particular those of AREQ) are fixed to accurate values, determined from a previous processing and the a priori coordinate constraints are loosed. The relative components of the baseline UAPF/AREQ are extracted from the daily solution with their uncertainties and organized as a time series giving the time history of the displacement of AREQ relative to UAPF.

[13] The site UAPF did not experience any measurable displacement during the coseismic phase of the 23 June earthquake, nor any transients during the postseismic phase [*Ruegg et al.*, 2001]. During the months or years preceding the main shock, the station UAPF as well as the station AREQ were affected by deformation due to interseismic loading along the subduction zone. At UAPF, the velocity is estimated to dE = 23.9 ± 0.4 mm/yr, dN = 5.43 ± 0.4 mm/yr with respect to stable South America.

[14] The position of the station AREQ with respect to stable South America, was calculated assuming a constant velocity at UAPF. If $[X_a(t) - Xu(t)]$ is the relative baseline component UAPF to AREQ, $X_a(t)$ being the position of AREQ in a given reference frame, we may write

$$X_a(t) = X_u(t_o) + V_u.(t - t_o) + [X_a(t) - X_u(t)], \qquad (1)$$

where $X_u(t_o)$ is the position of the station UAPF in the same reference frame at time t_o, V_u the interseismic velocity of UAPF as determined by *Bevis et al.* [1999] or by *Chlieh et al.* [2004], and $[X_a(t) - X_u(t)]$ the relative baseline component UAPF to AREQ issued from the GAMIT solution for time t. Figure 2 displays the displacement with respect to stable South America of the station AREQ during the period 2000.0 and 2003.5 projected on the direction N55°. As shown in Figure 2, our processing yields results consistent with those of *Melbourne and Webb* [2002]. The abrupt offset occurring on 23 June 2001 (phase CC′ on Figure 2) indicates a coseismic displacement toward the trench at AREQ, of about 0.5 m toward N235°E (Figure 2). Before the event, AREQ was moving away from the trench, as expected from strain accumulation along the trench in the interseismic period, almost linearly with time (phase AB). A departure from a linear trend (phase BC) is observed starting about 3–5 months before the event and was interpreted as evidence for preseismic slip [*Ruegg et al.*, 2001]. If we exclude this period, AREQ was moving by about 22 mm/yr relative to stable South America (Figure 3) in agreement with the estimate of *Melbourne and Webb* [2002] (Figure 2).

[15] The displacements recorded after the earthquake show first a one month period of rapidly decaying motion toward the trench (C′D). During this period the rate is high (of the order of a few mm/d). The strongest aftershock of 7 July (M_w = 7.6) produced in particular a visible signal of 2–3 cm on the time series at AREQ (point D). During the

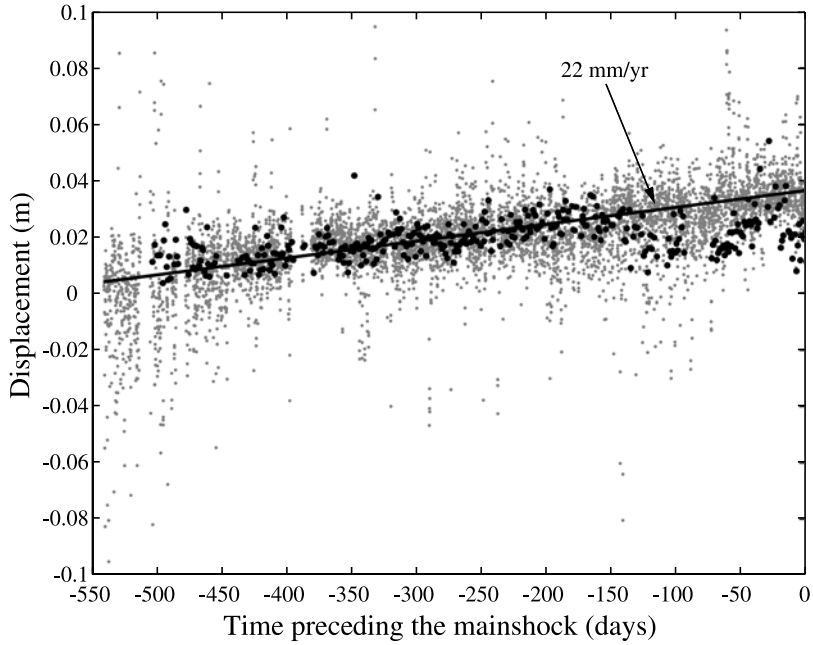

Figure 3. Preseismic displacement in the N55° direction at GPS station AREQ relative to South America (gray dots, *Melbourne and Webb* [2002]; black dots, this study). The velocity prior to the main shock is of the order of 22 mm/yr (black solid line).

last period (phase DE), covered by a two years record, the rate decreased more slowly to about 41 mm/yr (or 0.11 mm/d). Over that period, postseismic relaxation clearly dominates the signal at AREQ since the sense of motion is still trenchward, opposite to the sense of motion in the interseismic period. The postseismic displacement vector stays parallel to the coseismic displacement and at the end of the period of observation reaches 15 cm, i.e., about 30% of the coseismic signal at AREQ. Two years after the main shock the velocity vector of AREQ is still pointing toward the southwest, in the opposite direction of the interseismic loading.

4. Modeling Geodetic Displacements and Seismicity Rate Changes Due to Stress Transfers During the Seismic Cycle

[16] We analyzed the GPS record and the seismicity rate changes on the basis of a simple spring-sliders system described by *Perfettini and Avouac* [2004b] that simulate stress transfers during the seismic cycle taking into account both the zone of afterslip and viscous flow at greater depth. A more sophisticated model in three dimensions would be possible but difficult to constrain since the temporal evolution of deformation was only recorded at one GPS station. This model was initially designed to mimic stress variations and seismicity around continental thrust faults such as along the Himalaya or Taiwan, where it might be argued that temperature and pressure increase with depth controls a transition from rate weakening to rate strengthening, and finally to fully viscous flow [*Avouac*, 2003; *Perfettini and Avouac*, 2004a]. The principle is general [*Scholz*, 1990], and the model might also apply to subduction zones. The only major difference for a subduction earthquake is that the viscous coupling between the lower and upper plate might results from a localized ductile shear zone along the plate interface, or from a distributed deformation throughout the mantle wedge. We recall here the main features of the model and refer the reader to *Perfettini and Avouac* [2004b] for a more detailed description.

4.1. Description of the Springs and Sliders Model of Stress Transfer

[17] Each portion of the fault is modeled from one slider, the system being loaded by a constant force per unit length F (see Figure 4) [*Perfettini and Avouac*, 2004b]. The behavior of the system is determined from the constitutive laws and the equation of force balance on each slider. The displacement of slider i is noted δ_i, its velocity $V_i = d\delta_i/dt$, and the frictional stress is τ_i. The length of spring i is l_i^0 when the spring is at rest and its stiffness is noted k_i. The width (or downdip extent) of each fault zone is noted w_i, $i = 1, 3$. The stiffness k_1 of the seismogenic fault zone (SFZ) and k_2 of the BCFZ are related to their width w_1 and w_2 through the relation

$$k_i = G/w_i,\ i = 1, 2, \tag{2}$$

where G is the shear modulus.

4.1.1. Slider 1: The Seismogenic Fault Zone (SFZ)

[18] A rate-and-state friction law is ascribed to slider 1 [*Dieterich*, 1979; *Ruina*, 1983] as often assumed in seismic cycle models [*Rice*, 1993]. The frictional stress is

$$\tau_1(V_1(t), \theta_1(t)) = \sigma_1\left[\mu_1^* + a_1 \log\left(V_1(t)/V_*\right) + b_1 \log\left(\theta_1(t)/\theta_*\right)\right], \tag{3}$$

where σ_1, $V_1(t)$, and $\theta_1(t)$ are the normal stress, sliding velocity, and state variable, respectively, of slider 1 at time t.

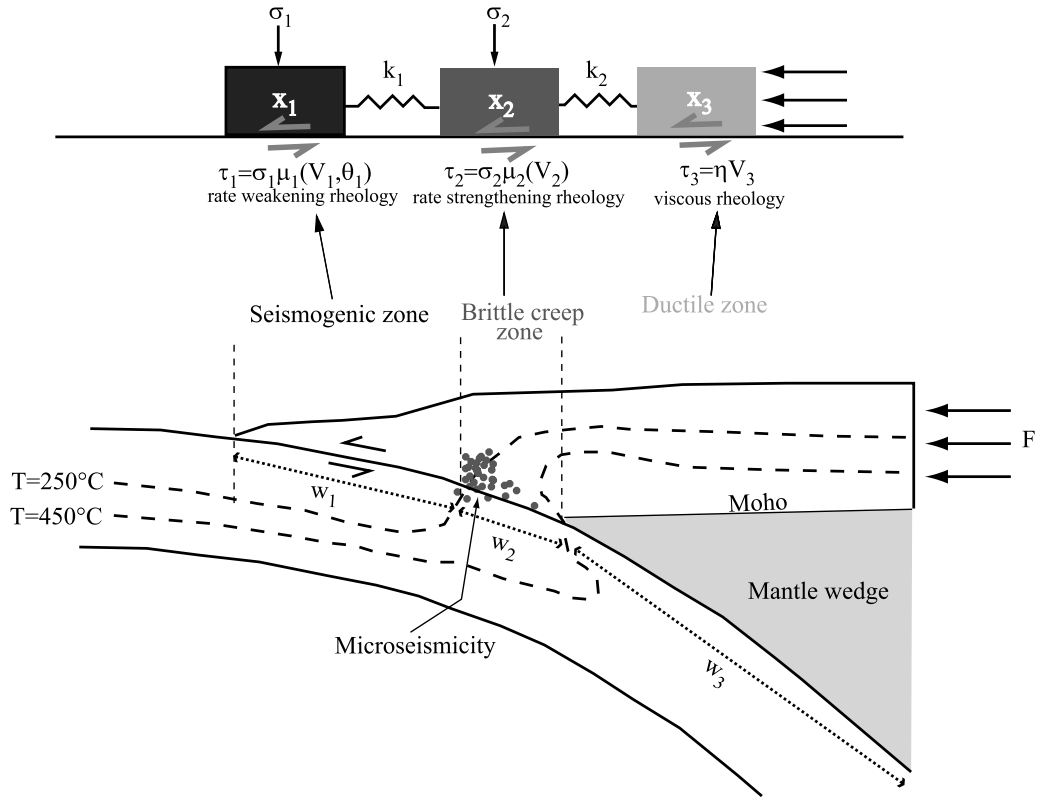

Figure 4. Fault model and 1-D springs and sliders model used in this study (see text for discussion).

The parameters a_1 and b_1 are empirical constants, while V_1^*, θ_1^* and μ_1^* are reference values such that $\tau_1(V_1^*, \theta_1^*)/\sigma_1 = \mu_1^*$. The state variable θ_1 follows the Dieterich (aging) law

$$\dot{\theta}_1 = 1 - \frac{V_1(t)\theta_1(t)}{D_c}, \tag{4}$$

where D_c, is a characteristic length. For slip instabilities to be possible, we assume a rate-weakening behavior, i.e., $a_1 < b_1$ [*Rice and Ruina*, 1983]. These slip instabilities are computed from a quasi-dynamic approximation [*Rice*, 1993] by writing

$$\frac{-GV_1}{2\beta} - k_1\left[(\delta_1 - \delta_2) - l_1^0\right] = \tau_1(V_1, \theta_1). \tag{5}$$

The first term is a radiation damping term which prevents infinite velocities during slip instabilities. It depends on the shear modulus G and the shear wave velocity β. We assume G = 30 GPa, and β = 3 km/s.

4.1.2. Slider 2: The Brittle Creep Fault Zone

[19] Slider 2 (BCFZ) is assumed to undergo rate-strengthening frictional sliding [*Perfettini and Avouac*, 2004a] with the frictional stress being

$$\tau_2(V_2(t)) = \sigma_2\left[\mu_2^* + a_2 \log\left(V_2(t)/V_*\right)\right], \tag{6}$$

where σ_2 and $V_2(t)$ are the normal stress and sliding velocity of slider 2, respectively, while μ_2^* and $a_2 > 0$ are empirical constants.

[20] The force balance on slider 2 implies

$$k_1\left[(\delta_1 - \delta_2) - l_1^0\right] - k_2\left[(\delta_2 - \delta_3) - l_2^0\right] = \tau_2(V_2). \tag{7}$$

4.1.3. Slider 3: The Ductile Fault Zone

[21] The shear stress τ_3 acting on slider 3 (ductile fault zone (DFZ)) is computed from

$$\tau_3(V_3) = \eta V_3, \tag{8}$$

where

$$\eta = \nu/\Delta h, \tag{9}$$

ν is the viscosity of the viscous layer, and Δh is the characteristic thickness of the viscous shear zone.

[22] The force balance on slider 3 implies

$$F = \tau_1(V_1, \theta_1)w_1 + \tau_2(V_2)w_2 + \tau_3(V_3)w_3, \tag{10}$$

F being the loading force per unit length.

4.2. Some Characteristic Features of the Model

[23] Figure 5 presents the slip of the different fault zones as a function of time for the set of parameters of Table 1 and a mean sliding velocity of the DFZ of V_0 = 79 mm/yr [*DeMets et al.*, 1990]. The model predicts the periodic return of the same event. The periodicity results from the 1-D assumption and of the fact that all sort of heterogeneities are neglected. In nature it is highly unlikely that these assumptions would hold, but some of the predictions of the model regarding relaxation and stress transfer might be relevant in spite of the simplifications made. The SFZ (black continuous line) presents a characteristic stick-slip

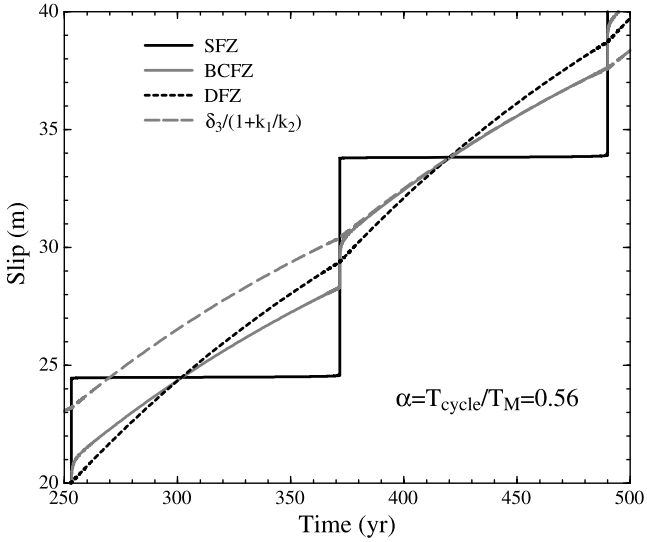

Figure 5. Slip of the various fault zones during the earthquake cycle for α = 0.56. The gray dashed line was obtained dividing the slip along the DFZ by the factor 1 + k_1/k_2 and shifting the curve vertically in order to compare it with slip along the BCFZ.

motion. The duration of the earthquake cycle T_{cycle} is given by

$$T_{\text{cycle}} = \frac{\Delta\tau}{k_1 V_0} = \frac{\Delta U}{V_0}, \tag{11}$$

where $\Delta\tau$ is the stress drop of the event, ΔU the total slip, and V_0 is the mean sliding velocity of the DFZ [*Perfettini and Avouac*, 2004b]. The stress drop of the event scales as $\Delta\tau \propto \sigma_1 (b_1 - a_1)$ [*Rice and Tse*, 1986].

[24] After each slip event along the SFZ the stress level in the BCFZ (gray continuous line) suddenly increases by some value of the order of the coseismic stress drop $\Delta\tau$ [*Perfettini and Avouac*, 2004b]. This stress transfer can be considered as almost instantaneous since the characteristic time t_r of the BCFZ is much larger than the duration of the coseismic phase (tens of seconds). Appendix A presents an analytical expression for the relaxation of the BCFZ. According to equation (A12) the velocity is increased by a factor $\exp[\Delta\tau/(a_2\sigma_2)]$ in response to the stress change $\Delta\tau$ and decays as $1/t$ with a characteristic time t_r given in equation (A4). During this phase, slip on the BCFZ increases logarithmically with time. After the transient postseismic response of the BCFZ, the evolution of slip on the BCFZ is constrained by slip along the DFZ (black dotted line). For steady sliding of the BCFZ ($\dot{V}_2 \simeq 0$, $V_1 \simeq 0$), the velocities of the BCFZ and DFZ are related through [*Perfettini and Avouac*, 2004b, equation (A2)]

$$V_2 = \frac{V_3}{1 + \frac{k_1}{k_2}}. \tag{12}$$

We see that relation (12) is quiet satisfactory except during the early postseismic relaxation of the BCFZ (Figure 5).

[25] The behavior of the DFZ depends on the parameter α [*Perfettini and Avouac*, 2004b]

$$\alpha = \frac{T_{\text{cycle}}}{T_M} = \log\left(\frac{V_3^+}{V_3^-}\right), \tag{13}$$

where the characteristic relaxation time of the DFZ (or Maxwell time) T_M is given by

$$T_M = \eta \frac{w_3}{w_1}\left(\frac{1}{k_1} + \frac{1}{k_2}\right), \tag{14}$$

and V_3^- and V_3^+ represents the sliding velocity of the DFZ immediately before and after the earthquake, respectively. In Appendix C we show that to a first approximation

$$V_3^- = \frac{\alpha}{\exp(\alpha) - 1} V_0 \tag{15}$$

$$V_3^+ = \frac{\alpha \exp(\alpha)}{\exp(\alpha) - 1} V_0. \tag{16}$$

When $\alpha \to 0$, the sliding velocity of the DFZ is constant with time with $V_3(t) \simeq V_0$, and the DFZ does not respond to the earthquake in the SFZ. In this case, our model is equivalent to a model loaded at constant velocity. Greater values of α leads to a jump in sliding velocity of the DFZ at the time of the earthquake. For instance when $\alpha \simeq 0.56$ such as in Figure 5, equation (13) predicts that $V_3^+/V_3^- \simeq 1.77$.

4.3. Predicting Geodetic Displacements

[26] Let $V(t)$ be the velocity at one geodetic station, say AREQ, in the N55° direction relative to South America. Let V_0 be the long-term convergence rate due to slip along the subduction interface, say the convergence rate of the South America plate relative to the Nazca plate, minus shortening of the continental margin. The velocity V' of station AREQ relative to the Nazca plate is given by

$$V'(t) = V_0 - V(t). \tag{17}$$

The velocity V' results from the contribution of the sliding velocity V_1 of the SFZ, the sliding velocity V_2 of the BCFZ and the sliding velocity V_3 of the DFZ. This can be stated as

$$V'(t) = g_1 V_1(t) + g_2 V_2(t) + g_3 V_3(t). \tag{18}$$

The constants g_1, g_2 and g_3 are geometrical factors that depends on the position and orientation of the station

Table 1. Parameters Used in the Numerical Model

Parameter	Value
G	30 GPa
β	3 km/s
μ_1^*	0.6
μ_2^*	0.6
a_1	4×10^{-3}
b_1	4.3×10^{-3}
D_c	0.01 m
V_*	10^{-10} m/s
a_2	5.7×10^{-4}
σ_1	300 MPa
σ_2	450 MPa
w_1	100 km
w_2	30 km
w_3	200 km
Δh	5 km
F	2.65 10^{13} N/m
V_0	79 mm/yr
T_{cycle}	120 years

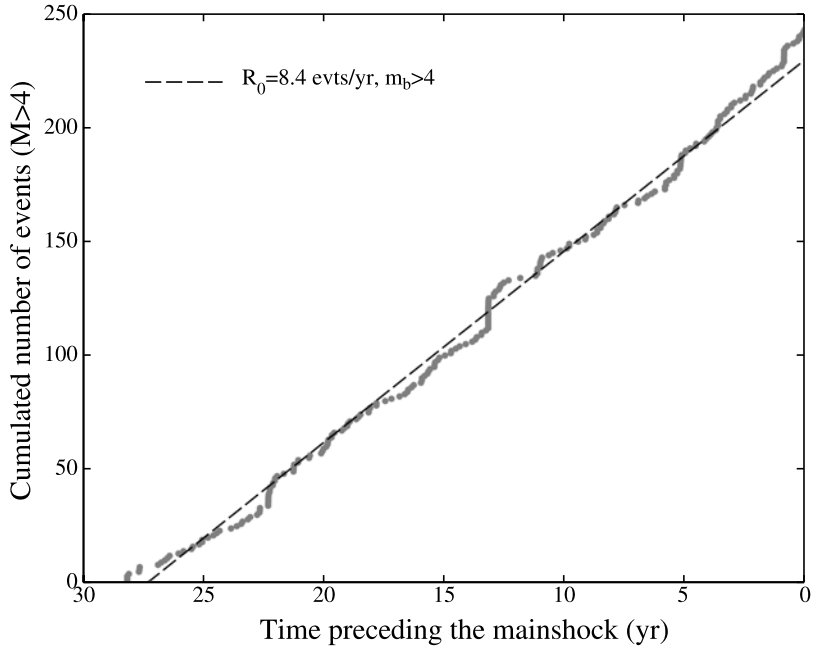

Figure 6. Cumulated number of events with $m_b > 4$ (NEIC catalog) prior to the south Peru earthquake in region A of Figure 1. The observed linear trend suggests a constant seismicity rate of the order of $R_0^- = 0.023$ events/d prior to the main shock.

relative to the SFZ, BCFZ and DFZ. These coefficients may be obtained using Green's functions computed from elastic dislocations in an elastic half-space as discussed in section 7.2. Necessarily, $0 < g_1 < 1$, $0 < g_2 < 1$, and $0 < g_3 < 1$, since only a fraction of slip on the fault is measured at the surface. The contribution of the SFZ can be neglected ($V_1 \simeq 0$) except during the coseismic phase. Noting that for a perfectly elastic medium $\langle V_1 \rangle = \langle V_2 \rangle = \langle V_3 \rangle = \langle V' \rangle = V_0$, where the angle brackets mean time average over an earthquake cycle, we get

$$g_1 + g_2 + g_3 = 1. \tag{19}$$

4.4. Evolution of Seismicity

[27] We make the simple assumption that the seismicity rate $R(t)$ is proportional to the sliding velocity $V_2(t)$ of the BCFZ. More or less we consider that seismicity reflects strain of the elastic medium surrounding the fault zone, but does not contribute significantly to strain release. The problem is to find the coefficient of proportionality between $R(t)$ and $V_2(t)$. This coefficient depends on various factors such as the size of the studied area, the cutoff magnitude of the catalog, the density of active faults in the region, their mechanical and constitutive properties, etc. If $R(t)$ is proportional to the sliding velocity $V_2(t)$ of the BCFZ, before the earthquake, the equality

$$\frac{R(t)}{R_0^-} = \frac{V_2(t)}{\left(V_2^0\right)^-}, \tag{20}$$

should hold, $(V_2^0)^-$ being the mean sliding velocity of the BCFZ during the years preceding the main shock. R_0^- represent the background seismicity before the earthquake.

[28] Using equation (12), we can relate $(V_2^0)^-$ to the sliding velocity V_3^- of the DFZ before the main shock

$$\left(V_2^0\right)^- = \frac{V_3^-}{1 + \frac{k_1}{k_2}}, \tag{21}$$

where k_1 and k_2 are the stiffness of the SFZ and BCFZ, respectively [*Perfettini and Avouac*, 2004b]. It follows that over most of the interseismic period, when equation (12) holds, the evolution of seismicity rate will be controlled by viscous loading. If α (see equation (13)) is small, the seismicity rate will be nearly uniform.

[29] In Appendix B we present an analytical derivation for the evolution of the seismicity rate in the postseismic phase. This derivation takes into account the possible acceleration of the DFZ. It is valid as long as the sliding velocity along the DFZ can be considered constant during the relaxation of the BCFZ, i.e., $T_M \gg t_r$. In particular, equation (B2) predicts that the background seismicity rate R_0^- before and R_0^+ after the earthquake are related through

$$\frac{R_0^+}{R_0^-} = \frac{\left(V_2^0\right)^+}{\left(V_2^0\right)^-} = \frac{V_3^+}{V_3^-} = \exp(\alpha), \tag{22}$$

where equations (12) and (13) have been used.

5. Testing the Compatibility of the Model With Observed Geodetic Relaxation and Aftershocks Rate Decay

[30] In this section we compare the observed seismicity rate change and the geodetic displacements at AREQ with

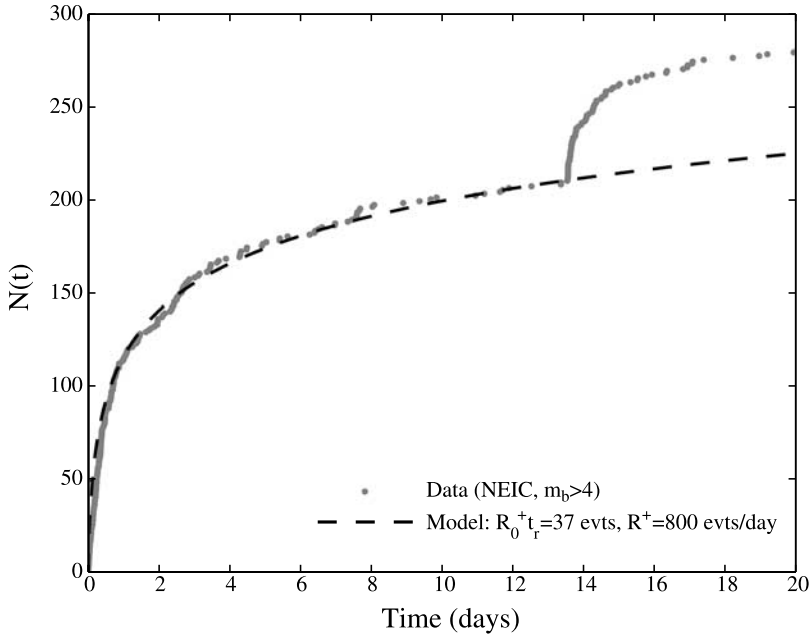

Figure 7. Cumulated number of events with $m_b > 4$ (NEIC catalog) following the south Peru earthquake in region A (see Figure 1 for location). The model assumes that seismicity rate change is controlled by deep afterslip computed from the response of a fault interface with rate-strengthening friction according to the analytical formulation that neglects contribution of viscous relaxation to reloading (equation (23)). This model predicts an Omori type of decay characterized by two parameters, $R_0^+ t_r$ and R^+.

analytical approximations to the solution of the springs and sliders model described above.

5.1. Seismicity Data

[31] Figure 6 shows the cumulated number of events with $m_b > 4$ as a function of time during the 10,000 days preceding the 2001 south Peru main shock in region A which corresponds to the black box in Figure 1. The data come from the NEIC catalog which is complete for magnitude above $m_b > 4$ in this area. We see that prior to the main shock, the cumulated number of events presents a linear trend. Therefore the seismicity rate appears to be approximately in steady state prior to the 2001 main shock. We will note this background value R_0^-. In region A, we found that $R_0^- \simeq 0.023$ events/d is a reasonable value during the 10,000 days preceding the main shock.

[32] Figure 7 presents the evolution of the cumulated number of aftershocks with $m_b > 4$ during the first 20 days following the 23 June 2001 event. Figure 8 shows the same data over 900 days. The effect of the 7 July aftershock is clearly visible on Figure 7, producing a second aftershock sequence. Since the overall response of the region we are studying (region A of Figure 1) is mainly controlled by the main shock, we will only consider the evolution of seismicity during the period preceding the 7 July aftershock. One of the goal of this work being to connect the evolution of seismicity with the evolution of afterslip, we see that the 7 July aftershock has a much weaker influence on displacement at station AREQ than the main shock (Figure 2).

[33] During the 13 days between the main shock and the 7 July aftershock, equation (B6) reduces to

$$N(t) \simeq N(0) + R_0^+ t_r \log\left[1 + \frac{R^+}{R_0^+ t_r} t\right], \qquad (23)$$

since over this period of observations, it is reasonable to assume $t \ll t_r$. Looking at equation (23), we see that there are two unknown quantities that might be adjusted to fit the data: the seismicity rate R^+ immediately after the main shock and the product $R_0^+ t_r$. The best fit (black dashed line) to the data (gray circles) yields $R_0^+ t_r \simeq 37$ events and $R^+ \simeq 800$ events/d. With such set of parameters, the analytical expression (23) provides a good fit to the first 2 weeks of aftershocks (Figure 7) and later in the process when the effect of the 7 July aftershock become negligible (Figure 8).

5.2. GPS Data

[34] The displacement $\delta(t)$ at any point in the medium is thought to reflect the combined effect of slip along the BCFZ and along the DFZ. Given that seismicity rate is assumed to mimic the time evolution of slip along the BCFZ and that to the first order, the sliding velocity due to viscous flow along the DFZ might be assumed constant, in section C1 we show that

$$\delta(t) = c_0 + \frac{V_{II}[N(t) - N(0)]}{R_0^-} + V_{III} t, \qquad (24)$$

where c_0, V_{II}, and V_{III} are three constants. Basically, equation (24) expresses that apart from the linear term V_{III} t (due to slip of the DFZ), seismicity and geodetic data have the same temporal evolution (due to slip of the BCFZ). Since the characteristic time T_M for evolution of the DFZ are expected to be much larger (hundreds of years or more) than our period of observation (few years), we assume that V_{III} is constant during the time interval considered here. By constant, we mean that V_{III} has a constant value, say V_{III}^-, during the preseismic phase, and an other constant value, say V_{III}^+, during the postseismic phase. Nevertheless and as

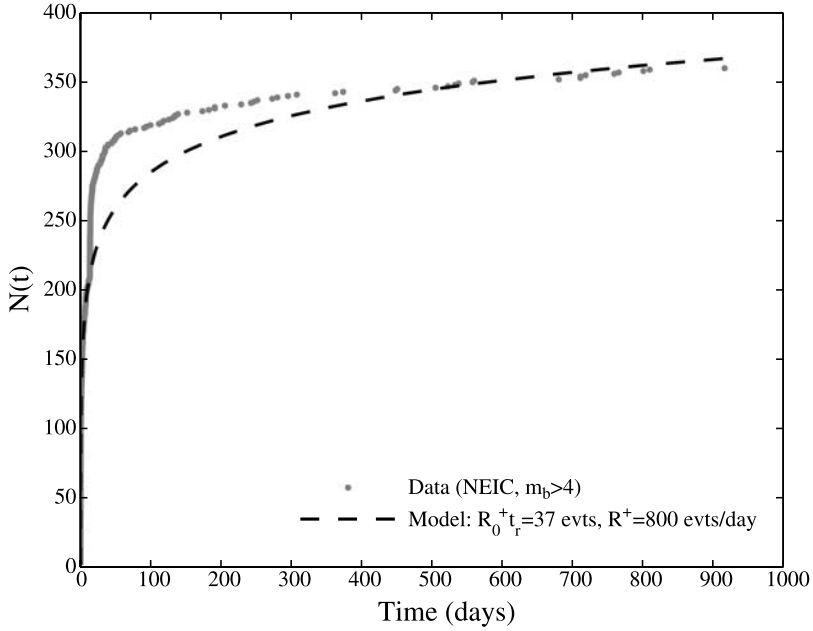

Figure 8. Same as Figure 7 over a longer postseismic period.

will be shown immediately below, $V_{III}^{+} \neq V_{III}^{-}$ since the occurrence of the main shock results in an instantaneous acceleration of the DFZ during the coseismic phase. Using the expression for the cumulated number $N(t)$ of earthquakes obtained in section 5.1, the best fit (gray continuous line) to the postseismic displacement at station AREQ (black circles) is obtained for $c_0 = -0.42$ m, $V_{II} = -5.1$ mm/yr and $V_{III} = -13$ mm/yr (Figure 9).

[35] In Appendix C, we relate the obtained values for $V_{II} = -5.1$ mm/yr and V_{III} to the characteristics of the DFZ. With the values of $V_{II} = -5.1$ mm/yr and $V_{III} = -13$ mm/yr, equation (C7) predicts that the sliding velocity

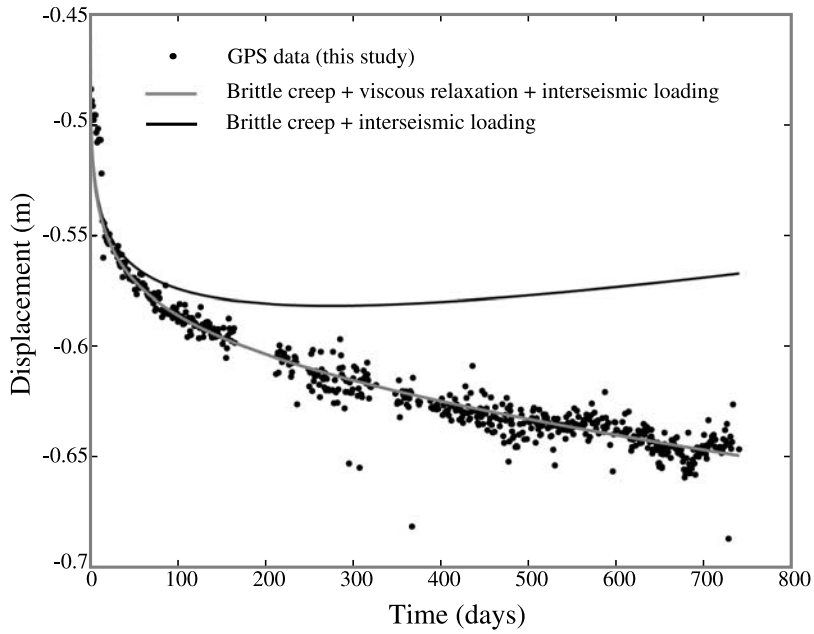

Figure 9. Postseismic displacement induced by the 23 June south Peru earthquake at station AREQ as a function of the cumulated number of events. The fit to the data (gray solid line) predicted by equation (24) (black solid circles) leads to $c_0 = -0.42$ m, $V_{II} = -5.1$ mm/yr and $V_{III} = -13$ mm/yr. This model assumes that both the geodetic displacement and the seismicity rate change are controlled by deep afterslip computed from the response of a fault interface with rate-strengthening friction. The GPS data require also a contribution from ductile relaxation. Indeed, the case where interseismic strain is assumed stationary (black solid line) yields a poor fit to the data ($V_{III} = 27.1$ mm/yr). The best fitting model implies a acceleration of viscous shear by a factor 1.77. See discussion in text.

of the DFZ increases by a factor $V_3^+/V_3^- \simeq 1.77$. The value of V_{III} that would be consistent with a constant sliding velocity of the DFZ throughout the earthquake cycle ($V_3^+ = V_3^-$) can be found using equation (C7), and leads to $V_{III} = V_L - V_{II} \simeq 27.1$ mm/yr. The model then departs significantly from the data (Figure 9), suggesting that viscous shear cannot be considered steady state over the seismic cycle. In other words, a significant viscous relaxation term is definitely needed.

[36] This analysis shows that within the framework of our model, the acceleration of viscous flow due to coseismic stress change must be taken into account to explain the observed displacements at AREQ. The temporal evolution of seismicity and geodetic displacements at station AREQ is thus consistent with the idea that postseismic relaxation would be essentially controlled by the intrinsic response of the BCFZ combined with reloading by viscous flow. The geodetic displacement in the early time of the postseismic relaxation seems to be controlled by the BCFZ, but as it gets relaxed, the loading of the DFZ should no longer be neglected. In section 6 we compare the data with the prediction of the numerical solution of the springs and sliders model.

6. Simulating Seismicity Rate and Geodetic Displacements Over the Seismic Cycle

6.1. Parameters of the Numerical Model for the 2001 South Peru Main Shock

[37] Here we describe the numerical solution of the springs and sliders model for a set of parameters that was adjusted to fit the geodetic and seismological observations. This allows assessment of the prediction of the model over a full seismic cycle, something that is not possible using the analytical approximations discussed in section 5.2.

[38] We sought for a set of parameters yielding a model consistent with the following constraints: (1) the average sliding velocity of the DFZ has to be of the order of $V_0 = 79$ mm/yr (NUVEL-1) (we neglect crustal shortening of the continental margin); (2) the recurrence time of a major subduction event is set to $T_{\text{cycle}} = 120$ years; (3) the model should lead to a preseismic velocity at station AREQ of the order of $V_L = 22$ mm/yr for, say, the last 2 years preceding the main shock; (4) the evolution of seismicity predicted by the model (see equation (20)) should reflect the observed seismicity; and (5) the postseismic phase should be in agreement with the evolution of postseismic slip at station AREQ.

[39] In Appendix D we derive, from analytical approximations, a set of initial parameters that fulfill requirements 1–5 that was next slightly adjusted by trial and error. The final set of parameters corresponding to our best guess is given in Table 1. Once constraints 1–5 are expressed, the number of free parameters is significantly reduced. Among those are the downdip extent w_1 of the SFZ. In fact this parameter seems to be reasonably well constrained to about $w_1 = 100$ km on the basis of kinematic inversion of seismological data [*Kikuchi and Yamanaka*, 2001] and by the aftershock distribution [*Tavera et al.*, 2002]. The parameters μ^*_1 and μ^*_2 have no influence on the dynamics of the system but only affects the level of the minimum force needed for the onset of motion [*Perfettini and Avouac*, 2004b]. The other free parameters are the effective normal stresses σ_1 and σ_2 acting on the SFZ and BCFZ, respectively. Even though the respective values of σ_1 and σ_2 are not constrained, the products $(b_1 - a_1)\sigma_1$ and $a_2\sigma_2$ have to be of the order of $(b_1 - a_1)\sigma_1 \simeq 0.09$ MPa and $a_2\sigma_2 \simeq 0.27$ MPa in order to match requirements 1, 2, and 4. The other model parameter constrained by the data is $\nu w_3/\Delta h \simeq 4.9 \times 10^{12}$ Pa yr. If this product is kept constant but the thickness, width, and viscosity of the viscous shear zone are changed accordingly, the prediction of the model are identical. If we assume that the viscous deformation is localized and choose, for instance, $\Delta h = 5$ km and $w_3 = 200$ km, we infer a viscosity of $\nu = 3.9 \times 10^{18}$ Pa s. If we assume that the deformation is accommodated over the whole mantle wedge and choose, for instance, $\Delta h = 100$ km and $w_3 = 500$ km, we find $\nu = 3 \times 10^{19}$ Pa s. Those two end-member cases provide reasonable inference of the viscosity of the viscous shear zone.

[40] It turns out that the five conditions listed above fully constrain the model. Extrapolating the evolution of the system over the seismic cycle is thus uniquely determined, although the uncertainties on the model parameters would allow some variability in the predictions. Figure 5 presents the slip of the various fault zones for the best fitting set of parameters of Table 1.

6.2. Computation of Displacement of GPS Station AREQ

[41] In order to model the displacement of station AREQ in the N55°E direction relative to South America, we first have to determine the geometric coefficients g_1, g_2 and g_3 (see equation (18)).

[42] Using the set of parameters from Table 1, we find $V_3^- = 59.6$ mm/yr and $V_3^+ = 101.5$ mm/yr, leading to $V_3^+/V_3^- = 1.7$, as estimated from the analytical approximations. Combining equation (C3) with (21), we find

$$g_2 = -\frac{V_{II}}{V_3^-}\left(1 + \frac{k_1}{k_2}\right). \tag{25}$$

Given that the data imply $V_{II} = -5.1$ mm/yr and $V_3^- = 59.6$ mm/yr, we find $g_2 = 0.11$.

[43] Using equation (C6), we find

$$g_3 = \frac{V_0 + V_{II} - V_L}{V_3^-}, \tag{26}$$

which using $V_L = 22$ mm/yr, leads to $g_3 \simeq 0.87$.

[44] Given that the total slip of the SFZ is of the order of $\Delta U \simeq 9.3$ m, and that coseismic displacements at stations AREQ was $\delta_{\text{cos}} \simeq 0.44$ m, we get,

$$g_1 = \frac{\delta_{\text{cos}}}{\Delta U} \simeq 0.047. \tag{27}$$

[45] The value $g_3 \simeq 0.87$ predicted by equation (26) leads to an average velocity at station AREQ of 2 mm/yr trenchward. In order to get rid of this drift, a value of $g_3 \simeq 0.84$ has to be used. Note that with the values found above, $g_1 + g_2 + g_3 \simeq 1.03$, which is in close agreement with the theoretical value of 1 predicted by equation (19).

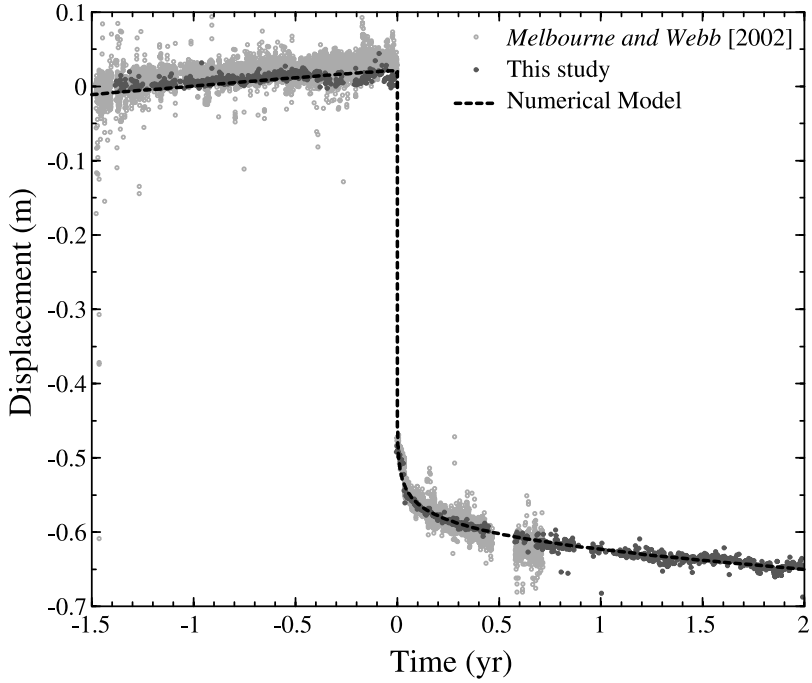

Figure 10. Displacement of station AREQ in the N55°E direction relative to South America predicted by the numerical model. The model (black dashed line) is able to describe the preseismic and postseismic slip at this GPS station.

[46] Figure 10 shows the prediction of the model using the value $g_1 \simeq 0.047$, $g_2 = 0.11$ and $g_3 = 0.84$ during the period covered by the GPS time series.

[47] Figure 11 shows the motion of GPS station AREQ over a few earthquake cycles. We see that the velocity at that point, relative to South America, varies all over the seismic cycle. roughly at the middle of the earthquake cycle. Such a feature is due to the significant acceleration of the DFZ in response to the main shock.

6.3. Seismicity Rate Change During the Seismic Cycle

[48] Figure 12 presents the evolution with time of the cumulated number of earthquakes ($m_b > 4$) following the main shock. The model (black continuous line) is

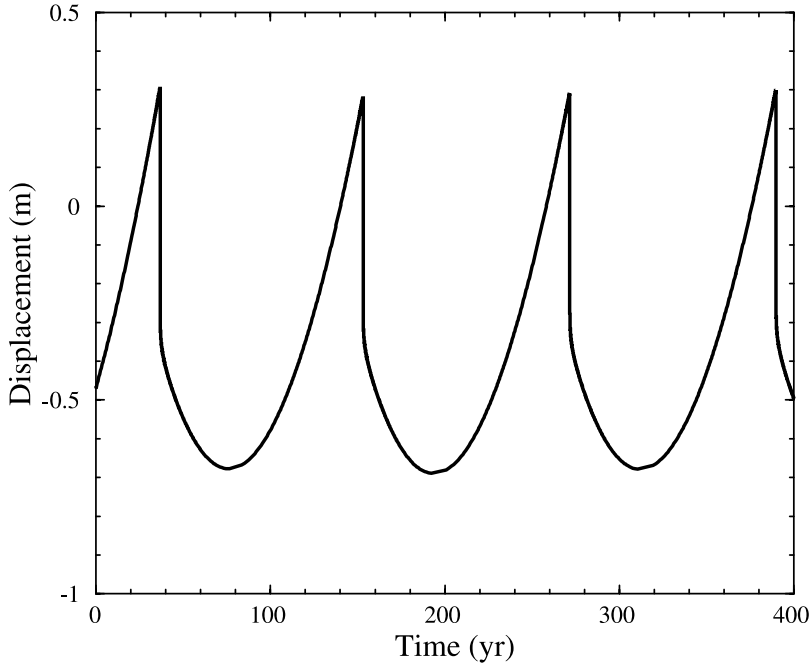

Figure 11. Same as Figure 10 but over several earthquake cycles. Note the reversal of the direction of motion due to the response of the DFZ.

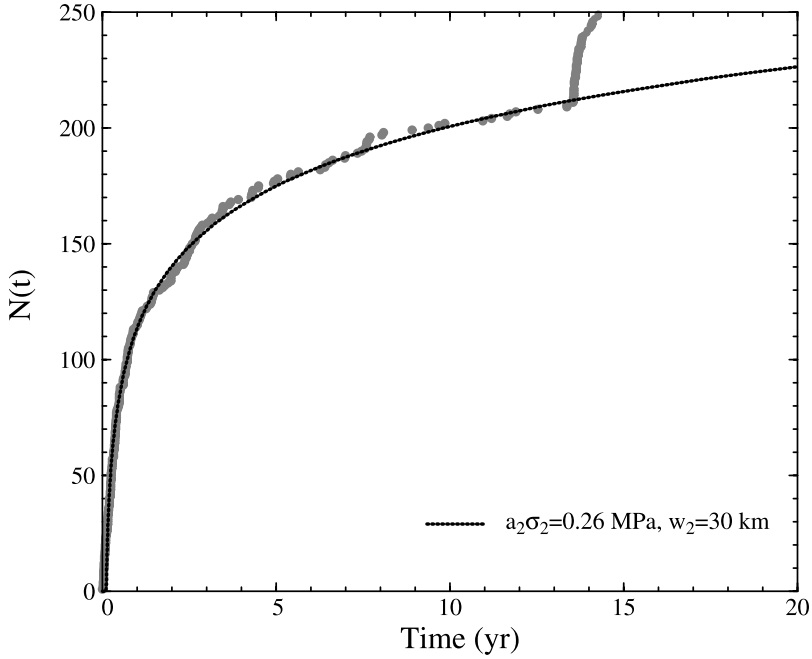

Figure 12. Evolution of the cumulated number of earthquakes with $m_b > 4$ (NEIC catalog) as a function of the time elapsed since the main shock. Continuous line shows the prediction of the spring-and-sliders model for the parameters listed in Table 1.

in close agreement with the data (gray circles). The model yields $a_2\sigma_2 \simeq 0.26$ MPa and $t_r = 2.56$ years. The background seismicity rate prior the main shock is $R_0^- \simeq 0.024$ events/d while the seismicity rate immediately after the main shock is of the order of $R^+ \simeq 770$ events/d. Therefore it can be considered that requirement 4 is fulfilled.

[49] Figure 13 presents the evolution of the cumulated number of events over two earthquake cycles. The Figure 13 inset shows a zoom around a typical earthquake. Before the event, the seismicity rate is equal to its long-term value R_0^-, jumping to R^+ at the time of the main shock. It then evolves toward it postearthquake background value R_0^+ once the BCFZ has fully relaxed. All along the cycle, the

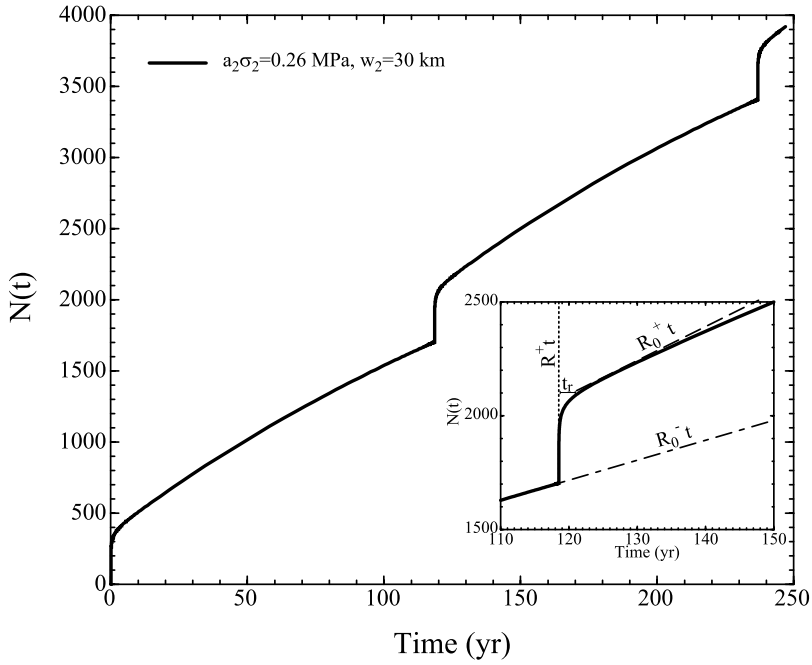

Figure 13. Variations of the cumulated number of earthquakes ($m_b > 4$) during the seismic cycle.

seismicity rate (slope of the curve) is changing with time due to the nonstationarity of the DFZ.

7. Discussion

7.1. Mechanism Associated With Postseismic Strain and Aftershocks

[50] The continuous GPS station at Arequipa provides an exceptional record of the temporal evolution of ground displacement associated with strain accumulation and release along the South America subduction zone. The record provides information on preseismic, coseismic and postseismic phases associated with the 2001 Peru event. The postseismic relaxation over the two years following the earthquake shows two phases of relaxation, both with trenchward motion opposite to the sense of motion during the interseismic phase. This record can be satisfyingly explained from a model in which coseismic stress drop is taken up by stress increase along the deeper portions of the plate interface characterized by rate-strengthening friction and viscous flow at greater depth. Rate-strengthening frictional sliding is dominant in the early postseismic relaxation phase, but a viscous response is also needed to account for the two phases relaxation process and the need for a reversal of sense of motion at some stage in the seismic cycle. This postseismic relaxation process must induce rapid reloading of the medium surrounding the DFZ and BCFZ, potentially driving aftershocks as suggested from the comparison of the temporal evolutions of the seismicity and GPS data.

[51] A Newtonian DFZ has been assumed in our 1-D model. Nevertheless, most of the results presented here remain valid considering a non-Newtonian DFZ. The main assumption made concerning the behavior of the DFZ is that its characteristic (or Maxwell time) was much larger than the relaxation time t_r of the BCFZ, so that the sliding velocity of the DFZ may be considered constant during the relaxation process of the BCFZ. Since t_r seems to be of the order of a few years [*Perfettini and Avouac*, 2004a], and given that the Maxwell time is of the order of hundreds of years or more [e.g., *Bills et al.*, 1994; *Cohen*, 1999]), this assumption seems quiet reasonable in nature. Results from Appendix A, B, C1, and C2 remains unchanged whether the DFZ has a Newtonian or non-Newtonian rheology. In Appendix C3, equation (C7) remains valid and fixes the ratio V_3^+/V_3^-. However, the estimate of the individual velocities V_3^+ and V_3^- are dependent on the rheology of the DFZ even though their ratio is not. In particular, equations (15) and (16) are no longer true for a non-Newtonian rheology of the DFZ. Looking at Appendix D, we can see the derivation of the parameters of the SFZ and BCFZ are not depending on the rheology of the DFZ. Since the individuals velocities V_3^- and V_3^+ may be different in the case of a non-Newtonian DFZ, the geometric coefficients g_2 and g_3 may also change. Nevertheless, the framework presented in this paper can be easily extended to any type of viscous rheology as long as the parameters of the DFZ fulfill the constrains $\langle V_3 \rangle = V_0$, $\langle V_3 \rangle$ being the mean sliding velocity of the DFZ averaged over one earthquake cycle, and $V_3^+/V_3^- \simeq 1.77$.

7.2. Significance of the Geometric Factors g_1, g_2, and g_3

[52] The motion at any point on the surface depends on the slip rate across the various portions of the plate interface, namely, the SFZ, BCFZ and DFZ. Three geometric factors have therefore been introduced and estimated from the fit to the GPS time series. They were determined independently of any geometric consideration but it is satisfying to see that their relative values make some sense. First, the fact that the larger geometric factor, g_3, corresponds to the DFZ makes sense given the position of the station well inland, which is about 250 km distant from the trench.

[53] For comparison we have computed those factors using Okada equations [*Okada*, 1992]. For this, we assume a dip angle of the subducting plate of 25° [*Tavera and Buforn*, 2001]. The along strike extension of the fault is set to 5000 km, an arbitrary value chosen to be large enough to avoid edge effects. The width of the SFZ and BCFZ are 100 km and 30 km, respectively, as in the 1-D model. We have assumed a width of the DFZ of 200 km in our 1-D model but in reality, we expect ductile flow to continue at much greater depth. Consequently, we have set the width of the DFZ to infinity. We then calculate the horizontal displacements induced at station AREQ (assumed to be 250 km distant from the trench) due to a slip of unity of the SFZ alone, the BCFZ alone, the DFZ alone, assuming a rake of 90°. The values obtained are $\delta U_{\mathrm{SFZ}} \simeq -0.137$ $\delta U_{\mathrm{BCFZ}} \simeq -0.0587$, and $\delta U_{\mathrm{DFZ}} \simeq -0.467$, respectively. The coefficients g_1, g_2 and g_3 are then computed using $g_1 = \delta U_{\mathrm{SFZ}}/\Sigma U$, $g_2 = \delta U_{\mathrm{BCFZ}}/\Sigma U$ and $g_3 = \delta U_{\mathrm{DFZ}}/\Sigma U$, where $\Sigma U = \delta U_{\mathrm{SFZ}} + \delta U_{\mathrm{BCFZ}} + \delta U_{\mathrm{DFZ}}$. Those values leads to $g_1 \simeq 0.21$, $g_2 \simeq 0.09$, and $g_3 \simeq 0.7$. The values of g_2 and g_3 obtained are comparable to the values inferred from our 1-D model (0.11 and 0.87, respectively), but the coefficient g_1 differs significantly from our estimate (0.047). In fact, and as discussed in Appendix D, our 1-D model overestimates the coseismic slip of the event, which was found to be of the order of 9.5 m. If we use a mean coseismic slip of 2 m as suggested by J.-C. Ruegg et al. (unpublished manuscript, 2002), we found using equation (27) that $g_1 \simeq 0.22$. This value is in close agreement with the prediction $g_1 \simeq 0.21$ obtained considering elastic dislocation theory.

[54] Finally, it is very satisfactory to see that the ratio g_3/g_2 predicted by elastic dislocation theory yields $g_3/g_2 \simeq 7.97$, while our 1-D model predicts $g_3/g_2 \simeq 7.9$. This shows that the relative contribution of the BCFZ and DFZ to the postseismic relaxation process predicted by our 1-D model only depends on the geometry of the various fault zones and on the position of the GPS station.

7.3. Possibility of Significant Strain Rate Variation Over the Seismic Cycle

[55] The model predicts that the geodetic strain along the trench might be far from stationary over the seismic cycle. At station AREQ, our model predicts that velocity relative to South America should remain trenchward over about 40 years and then reverse to landward direction (Figure 11). Such a feature is due to the response of the DFZ which velocity is increased by a factor 1.7 due to the occurrence of the main shock. Since T_M is almost two times larger than the duration of the earthquake cycle, the DFZ cannot fully relax between two successive large earthquake. This implies that geodetic measurements made at various stages of the seismic cycle would presumably yield very different results regarding the estimated convergence rate or the degree of

coupling of the plate interface. This shows that stress transfer during the seismic cycle might induce significant temporal variation of strain rate during the whole period between two successive large earthquakes. This effect is also visible in the predicted seismicity rate (Figure 13). Indeed, the evolution of the background seismicity, once the transient brittle creep response is over, follows an evolution dictated by the DFZ, and decay by a factor of about 1.7 over about 1 century.

7.4. Values of the Parameters $a_2\sigma_2$, a_2, σ_2, and t_r

[56] By adjusting the model parameters to the data from the 2001 Peru earthquake we have obtained $a_2\sigma_2 \simeq 0.26$ MPa. For comparison, *Perfettini and Avouac* [2004a] found $a_2\sigma_2 = 0.34-1.5$ MPa in the case of the Chi-Chi earthquake. The middle of the BCFZ being at a downdip extent of 115 km in our model, and knowing that the dip angle of the subducting plate is of the order of 25° [*Tavera and Buforn*, 2001], we find that the average depth of the BCFZ is of the order of 50 km. The mean effective normal stress of the BCFZ is presumably of the order of $\sigma_2 = 600-1000$ MPa if pore pressure is hydrostatic or less. Since $a_2\sigma_2 \simeq 0.26$ MPa, this leads to $a_2 = 2.6 \times 10^{-4}-4 \times 10^{-4}$. These values are 1 to 2 orders of magnitude lower than those estimated from laboratory experiments on wet granite and wet quartz gouge which fall in the range $a_2 = 5 \times 10^{-3}-0.03$ for temperatures greater than 300°C [*Blanpied et al.*, 1995; *Chester*, 1995], which is approximately the temperature range in the BCFZ.

[57] If we set $a_2 = 5 \times 10^{-3}-0.03$, a value consistent with laboratory measurement, we get $\sigma_2 \simeq 9-52$ MPa. Such a small effective normal stress is nearly 2 order of magnitudes lower than the lithostatic pressure at this depth. It may be possible that very high pore pressure would be associated with the BCFZ, since the corresponding temperature range is susceptible of producing various dehydration reactions that could affect the subducting slab and the sediments dragged along the plate interface. Another possibility is that low effective normal stress along the BCFZ may results from the negative buoyancy of the subducting slab [*Scholz and Campos*, 1995].

[58] Our model predicts a relaxation time of the BCFZ of the order of $t_r \simeq 2.6$ years. This value is comparable to but smaller than the value of $t_r = 8.5$ years found by *Perfettini and Avouac* [2004a] for the 1999 Chi-Chi earthquake. Since $t_r = a_2\sigma_2/(k_2V_3^+)$, the difference of the relaxation time may result form both the smaller value of $a_2\sigma_2$ in the case of the Peru subduction zone and a larger convergence rate.

7.5. Reversal Time t_i

[59] In section C4, we give an estimate of the time t_i where a GPS station reverse its direction of motion. This leads to

$$t_i = T_M \log\left[\frac{\bar{g}}{1+\exp(-\alpha)}\right], \tag{28}$$

where

$$\bar{g} = g_3 + \frac{g_2}{1+\frac{w_2}{w_1}}. \tag{29}$$

This simple expression shows that t_i depends only on the Maxwell time T_M, the ratio $\alpha = T_{\text{cycle}}/T_M$, and on the geometry. The ratio t_i/T_M increases with the distance from the trench through the parameter g_3. With the set of parameters used in this study ($T_M = 210$ years, $\alpha = 0.56$, $g_3 = 0.87$, $g_2 = 0.11$, $w_1 = 100$ km and $w_2 = 30$ km), we found $t_i \simeq 40.9$ years, a value in very good agreement with the results of Figure 11. For a station further away from the trench ($g_3 \rightarrow 1$ and $g_2 \rightarrow 0$), we found $t_i \simeq 50.7$ years.

[60] No reversal of the displacement of a GPS station is expected when $\bar{g} < 1 + \exp(-\alpha)$, since in this case, equation (28) leads to a negative time. Looking at equation (28), we see that this occurs for low values of g_3, i.e., when the station is close to the trench. Therefore a reversal of the direction of motion is expected only for inland stations, while coastal stations should not show such a feature.

7.6. Comparison With Other Large Subduction Earthquakes

[61] Recent GPS measurements by *Khazaradze et al.* [2002] show that sites 300–400 km landward of the rupture region of the 1960 ($M_w = 9.5$) great Chile earthquake moves seaward relative to stable South America, rather than landward as might be expected if interseismic strain was uniform. This requires that at some point, the direction of displacement at these sites will necessarily reverse to become landward. That reversal may happen as late as a few decades after the event pointing to a Maxwell time probably of the same order of magnitude as that proposed for the Peru subduction zone. Our estimate of this reversal time (up to 50.7 years based on equation (28) for our model parameters) is consistent with those observations. Similar observations were made by *Freymueller et al.* [2000] following the 1964 ($M_w = 9.2$) Alaska earthquake, where sites of seaward velocities were still observed at the end of the last century. In this particular case, it has also been proposed that the earthquake was followed by an early postseismic response decaying as $1/t$ dominant over a time constant of a few years [*Cohen*, 1998], possibly due to aseismic slip along a downdip extension of the coseismic rupture plane [*Brown et al.*, 1977], superimposed over another relaxation process with a time constant longer than the few decades covered by the data [*Savage and Plafker*, 1991]. Those observations are consistent with our model. Indeed we predict that during the first years following the main shock, the postseismic response is governed by the BCFZ as long as $t < t_r$. During this phase strain rate and seismicity rate decays simultaneously as $1/t$ due the velocity strengthening rheology of the BCFZ [*Perfettini and Avouac*, 2004a]. At subsequent times, the postseismic response if governed by the DFZ which characteristic relaxation time is much longer as illustrated by the value of 250 years we found.

8. Conclusion

[62] The simple 1-D model presented here captures the main features of the evolution of deformation and seismicity before and after the $M_w = 8.4$, 23 June 2001 Arequipa earthquake. The model parameters are well constrained from the evolution of seismicity and displacement measured at station AREQ during the 1.5 years before and the 2 years

after the Arequipa event. The model allows us to compute the evolution of displacement at station AREQ and seismicity throughout the earthquake cycle. Among the features observed, we predict an acceleration of the DFZ, its velocity before the main shock being 1.7 times larger than before the event. This requires a Maxwell time of the order of 210 years, a value larger than the estimated 120 years recurrence time of large earthquakes in this region. Subsequently, the DFZ does not have time to fully relax from the last earthquake when the next one occurs. It implies that background seismicity rates and geodetic strain rates are likely to vary significantly during the interseismic period, resulting in a possible persistent seaward motion, opposite to the preseismic motion, of inland stations as was observed following the 1960 (M_w = 9.5) great Chile earthquake and following the 1964 (M_w = 9.2) Alaska earthquake.

[63] This simplistic 1-D model allowed us to derive some analytical expressions in good agreement with the data (see Appendix A–C). They can be used to derive quickly some initial values of the constitutive parameters to be used in 3-D modeling of the seismic cycle based on a three fault zones model (SFZ, BCFZ, and DFZ). In particular, we could get a rough estimate of the ratio of the force drop $w_1\Delta\tau$ associated with coseismic stress drop on the SFZ to the force $F - F_c$ in excess of the frictional strength F_c of the system is $w_1\Delta\tau/(F - F_c) = \alpha(1 + w_2/w_1) \simeq 2.3$ [see *Perfettini and Avouac*, 2004b, equation (19)]. Obviously, this estimate would need to be reassessed on the basis of a more physical model of the dynamic interactions between the upper and lower plates in a subduction zone [e.g., *Buiter et al.*, 2001]. However, it is interesting to point out that our analysis would allow some estimate of the partitioning between frictional and viscous forces transmitted along the plate interface. If we assume a total stress drop that represents a fraction $\gamma < 1$ of the shear stress along the SFZ, we get that the coseismic force drop $w_1\Delta\tau$ is smaller than γF_c. Using $w_1\Delta\tau/(F - F_c) \simeq 2.3$, we found that F_c/F must be larger than $2.3/(\gamma + 2.3) > 70\%$.

Appendix A: Response of the BCFZ to a Sudden Slip Event in the SFZ

[64] With the use of equation (7), we find that the stress acting on the BCFZ immediately before the main shock is given by

$$k_1\left[\left(\delta_1^- - \delta_2^-\right) - l_1^0\right] - k_2\left[\left(\delta_2^- - \delta_3^-\right) - l_2^0\right] = \tau_2\left(V_2^-\right), \qquad \text{(A1)}$$

where the subscript number refers to the value of the variables at time $t = 0^-$. At any time t after the earthquake, the stress of the BCFZ is given by

$$\tau_2(V_2)(t) = k_1\left[\left(\delta_1^+ - \delta_2(t)\right) - l_1^0\right]_2(t) - \delta_3(t)) - l_2^0], \qquad \text{(A2)}$$

where equation (7) has been used noting that the slip of the SFZ is constant after the earthquake and equal to $\delta_1^+ = \Delta U + \delta_1^-$, ΔU being the final coseismic slip of the event.

[65] During the relaxation phase of the BCFZ, we assume that the sliding velocity of the DFZ is roughly constant and equal to V_3^+, leading to $\delta_3(t) \simeq \delta_3^- + V_3^+ t$. Such an assumption seems justified noting that the characteristic relaxation time of the DFZ is of the order of a hundred years or more.

[66] Subtracting equation (A2) from (A1) leads to

$$a_2\sigma_2 \log\left[\frac{V_2(t)}{V_2^-}\right] = -(k_1 + k_2)\left[\delta_2(t) - \delta_2^-\right] \qquad \text{(A3)}$$

where $\Delta\tau = k_1\Delta U$ is the static stress drop of the earthquake. Introducing the relaxation time t_r

$$t_r = \frac{a_2\sigma_2}{k_2 V_3^+}, \qquad \text{(A4)}$$

the amplification factor d

$$d = \exp\left(\frac{\Delta\tau}{a_2\sigma_2}\right), \qquad \text{(A5)}$$

and the parameter β

$$\beta = \frac{a_2\sigma_2}{k_1 + k_2}, \qquad \text{(A6)}$$

Equation (A3) leads after an integration with respect to time to

$$\delta_2(t) = \delta_2^- + \beta \log\left[1 + \frac{dV_2^- t_r}{\beta}(\exp(t/t_r) - 1)\right]. \qquad \text{(A7)}$$

At large times, the displacement of the BCFZ is given by

$$\lim_{t \gg t_r} \delta_2(t) = \frac{\beta}{t_r} t = \frac{V_3^+}{1 + \frac{k_1}{k_2}} t. \qquad \text{(A8)}$$

Therefore, when relaxing, the BCFZ tends to the sliding velocity $(V_2^0)^+$ given by

$$\left(V_2^0\right)^+ = \frac{V_3^+}{1 + \frac{k_1}{k_2}}, \qquad \text{(A9)}$$

which depends on the velocity of the DFZ prior to the earthquake. Note that equation (A9) is in agreement with equation (12) derived for steady slip of the BCFZ. It is important to note that the sliding velocity V_2^+ of the BCFZ immediately after the earthquake is different from $(V_2^0)^+$, which is the asymptotic velocity that will be reached at the end of the relaxation process of the BCFZ.

[67] Equations (A8) and (A9) may be combined to infer

$$\beta = t_r\left(V_2^0\right)^+. \qquad \text{(A10)}$$

Using equation (A10), we may write (A7) in an alternative form

$$\delta_2(t) = \delta_2^- + t_r\left(V_2^0\right)^+ \log\left[1 + \frac{dV_2^-}{\left(V_2^0\right)^+}(\exp(t/t_r) - 1)\right]. \qquad \text{(A11)}$$

The sliding velocity of the BCFZ can be obtained after differentiating equation (A11) with respect to time

$$V_2(t) = \frac{dV_2^- \exp(t/t_r)}{\left[1 + \frac{dV_2^-}{(V_2^0)^+}(\exp(t/t_r) - 1)\right]}, \qquad \text{(A12)}$$

and its value immediately the earthquake is $V_2(t = 0^+) = dV_2^-$. Therefore at the time of the earthquake, the velocity of the BCFZ is amplified by a factor d.

[68] To resume the features of this model. At the time of the earthquake, the sliding velocity is increased by a factor d, jumping from V_2^- to $V_2^+ = dV_2^-$, and further decreases over a time t_r to reach the asymptotic value $(V_2^0)^+$, which depends on the sliding velocity of the DFZ immediately after the earthquake. An assumption that we have made is that during the relaxation process of the BCFZ, the sliding velocity of the DFZ is constant and equal to V_3^+. Such an assumption is true if the Maxwell time T_M is much larger than t_r, i.e., $T_M \gg t_r$, which seems to be generally the case [*Perfettini and Avouac*, 2004a, 2004b]. When this hypothesis is violated, the analytical derivation above has to be reconsidered.

Appendix B: Changes in Seismicity Induced by the Slip of the BCFZ

[69] Using equations (20) and (A12), we can infer the seismicity rate after the earthquake

$$R(t) = \frac{R_0^-}{(V_2^0)^-} \frac{dV_2^- \exp(t/t_r)}{\left[1 + \frac{dV_2^-}{(V_2^0)^+}(\exp(t/t_r) - 1)\right]}. \quad \text{(B1)}$$

Using equation (20), we can find the background seismicity rate R_0^+ after the earthquake

$$R_0^+ = \frac{(V_2^0)^+}{(V_2^0)^-} R_0^-, \quad \text{(B2)}$$

and the seismicity rate R^- immediately before the earthquake

$$R^- = \frac{V_2^-}{(V_2^0)^-} R_0^-. \quad \text{(B3)}$$

According to equation (B1), the seismicity rate $R^+ = R(t = 0^+)$ immediately after the earthquake is given by

$$R^+ = \frac{R_0^- dV_2^-}{(V_2^0)^-} = dR^-. \quad \text{(B4)}$$

Using equations (B1)–(B4), we get a simplified expression for the seismicity rate

$$R(t) = \frac{R^+ \exp(t/t_r)}{\left[1 + \frac{R^+}{R_0^+}(\exp(t/t_r) - 1)\right]}. \quad \text{(B5)}$$

The cumulate number of earthquakes $N(t)$ at time t may be obtained integrating equation (B5) with respect to time

$$N(t) = N(0) + R_0^+ t_r \log\left[1 + \frac{R^+}{R_0^+}(\exp(t/t_r) - 1)\right], \quad \text{(B6)}$$

where $N(0)$ is the cumulated number of events prior to the earthquake.

Appendix C: Determination of the Properties of the DFZ

C1. Fit to the Postseismic Phase

[70] Using equations (17), (18) together with (20) and noting that during the postseismic phase the velocity $V_1(t)$ of the SFZ is negligible leads to

$$V(t) = V_0 - g_2 \frac{(V_2^0)^-}{R_0^-} R(t) - g_3 V_3(t). \quad \text{(C1)}$$

After integration with respect to time, equation (C1) becomes

$$\delta(t) = \delta(0) - g_2 \frac{(V_2^0)^-}{R_0^-}[N(t) - N(0)] + (V_0 - g_3 V_3^+)t, \quad \text{(C2)}$$

where $\delta(0)$ is the displacement of the GPS station and $N(0)$ the cumulated number of aftershocks at the time $t = 0$ of the main shock. In equation (C2), we have implicitly assumed that the velocity of the DFZ during the postseismic phase was $V_3^+ = V_3(t = 0^+)$, a value which can be considered constant during the 2 years of postseismic observation if the characteristic (or Maxwell) relaxation time T_M of the DFZ is much greater than the relaxation time t_r of the BCFZ. Equation (C2) is similar to (24) if

$$g_2 = -\frac{V_{II}}{(V_2^0)^-} \quad \text{(C3)}$$

$$V_{III} = V_0 - g_3 V_3^+. \quad \text{(C4)}$$

C2. Fit to the Preseismic Phase

[71] Let us note V_L the preseismic velocity measured at station AREQ relative to South America. Before the main shock, the sliding velocity of the BCFZ is $(V_2^0)^-$, and as in the postseismic phase, $V_1(t) \simeq 0$. Using equation (C1) in the preseismic phase where $R(t) = R_0^-$ yields

$$V_L = V_0 - g_2 (V_2^0)^- - g_3 V_3^-, \quad \text{(C5)}$$

where $V_3^- = V_3(t = 0^-)$ is the sliding velocity of the DFZ prior to the earthquake. Equation (C5) yields, after use of equation (C3)

$$V_L = V_0 + V_{II} - g_3 V_3^-. \quad \text{(C6)}$$

C3. Sliding Velocity of the DFZ Before and After the Main Shock

[72] In order to infer the properties of the DFZ, we first estimate the ratio V_3^+/V_3^-. Combining equations (C4) and (C6), we found

$$\frac{V_3^+}{V_3^-} = \frac{V_0 - V_{III}}{V_0 + V_{II} - V_L}. \quad \text{(C7)}$$

Using $V_L = 22$ mm/yr, $V_{II} = -5.1$ mm/yr and $V_{III} = -13$ mm/yr, we found $V_3^+/V_3^- \simeq 1.77$ or $\alpha \simeq 0.57$ (see equation (13)).

[73] We can now try to infer the individual velocities V_3^- and V_3^+. During the interseismic phase, *Perfettini and Avouac* [2004b] found that the velocity of the DFZ is given by

$$V_3(t) = V_3^+ \exp(-t/T_M), \tag{C8}$$

where again $V_3(t=0) = V_3^+$ is the sliding velocity of the DFZ immediately after the earthquake. Since V_0 is the mean sliding of the DFZ, using equation (C8), we get

$$V_0 = \frac{1}{T_{\text{cycle}}} \int_0^{T_{\text{cycle}}} V_3(t)\, dt = \frac{V_3^+}{\alpha}[1 - \exp(-\alpha)], \tag{C9}$$

with $\alpha = T_{\text{cycle}}/T_M$. Equation (C9) leads to

$$V_3^+ = \frac{\alpha \exp(\alpha)}{\exp(\alpha) - 1} V_0, \tag{C10}$$

and combining (13) together with (C10) yields

$$V_3^- = \frac{\alpha}{\exp(\alpha) - 1} V_0. \tag{C11}$$

C4. Estimation of the Reversal Time t_i

[74] We give here an estimation of the time t_i where the GPS station reverses its direction of motion. At time t_i, the velocity of the GPS station verifies $V(t_i) = 0$. Using equations (17) and (18) with $V_1(t) = 0$, we get

$$V_0 - g_2 V_2(t_i) - g_3 V_3(ti) = 0. \tag{C12}$$

Combining equation (12) which is valid once the BCFZ has relaxed (times greater than t_r) with equation (C12), we get

$$V_3(t_i) = \frac{V_0}{\bar{g}}, \tag{C13}$$

where the geometrical factor $\bar{g}$ is given by

$$\bar{g} = g_3 + \frac{g_2}{1 + \frac{w_2}{w_1}}. \tag{C14}$$

Using equation (C8) at time t_i together with equation (C10), we finally found

$$t_i = T_M \log\left[\frac{\bar{g}}{1 + \exp(-\alpha)}\right]. \tag{C15}$$

Appendix D: Determination of the Model Parameters

[75] We sought for a set of parameters consistent with the constraints 1–5 of section 6.1.

[76] According to equation (11), requirements 1 and 2 impose the coseismic slip to be $\Delta U \simeq 9.5$ m. Therefore a 1-D model intrinsically overestimates the coseismic slip which was estimated to be of 2.8 m on the basis of seismological data [*Kikuchi and Yamanaka*, 2001] or 2 m on the basis of GPS measurements (J.-C. Ruegg et al., unpublished manuscript, 2002).

[77] We further impose the downdip extent of the SFZ to be $w_1 = 100$ km. Imposing w_1 fixes the stiffness k_1 (equation (2)) and according to equation (11), the stress drop of the main shock is $\Delta\tau = k_1 \Delta U \simeq 2.8$ MPa. This value is a reasonable estimate though larger than the 1.9 MPa proposed by *Kikuchi and Yamanaka* [2001]. Because the dynamic of our model is controlled by stress transfers (and not slip transfers), the overestimate of coseismic slip is not crucial as long as the predicted stress drop is in agreement with the observations. Since $\Delta\tau \propto (b_1 - a_1)\sigma_1$ [*Rice and Ruina*, 1983], imposing the stress drop fixes the product $(b_1 - a_1)\sigma_1$ to 0.09 MPa. We arbitrary fix the effective normal stress of the SFZ to $\sigma_1 = 300$ MPa and $a_1 = 4 \times 10^{-3}$. As long as $(b_1 - a_1)\sigma_1 \simeq 0.09$ MPa, another combination of values for σ_1 and a_1 would not affect requirements 1 and 2.

[78] The mean sliding velocity of the DFZ has to be of the order of $V_0 = 79$ mm/yr. We have seen in the previous section that in order to fulfill requirements 1, 2, and 5 the jump of the sliding velocity of the DFZ has to be of the order of $V_3^+/V_3^- \simeq 1.77$. According to equation (13), this fixes $\alpha = \log(V_3^+/V_3^-) \simeq 0.57$ and the Maxwell time to be $T_M = T_{\text{cycle}}/\alpha \simeq 210.2$ years. Using equations (C10) and (C11), we find $V_3^- \simeq 58.5$ mm/yr and $V_3^+ \simeq 103.5$ mm/yr.

[79] We constrain the properties of the BCFZ so that the evolution of seismicity given by equation (20) predicted by the model is in agreement with the observed seismicity. In section 5.1, we found $R^+ \simeq 800$ events/d, while $R^- \simeq R_0^- \simeq 0.023$ events/yr, leading to an amplification of the seismicity rate at the time of the main shock of $d = R^+/R^- \simeq 3.48 \times 10^4$. Equation (A5) predicts that $a_2\sigma_2 = \Delta\tau/\log(d)$. Using the value $\Delta\tau \simeq 2.8$ MPa found earlier, leads to $a_2\sigma_2 \simeq 0.27$ MPa. According to equation (22), the seismicity rate after the main shock will relax to the background rate $R_0^+ = R_0^-\ (V_3^+/V_3^-) \simeq 0.04$ events/d. Using the value $R_0^+ tr \simeq 37$ events found in section 5.1, this yields $t_r \simeq 2.53$ years. Using equations (A4) and (2), we find $w_2 = GV_3^+ t_r/(a_2\sigma_2)$, which using the values found above leads to $w_2 \simeq 29.1$ km. According to equation (2), imposing w_2 fixes k_2. We impose the effective normal stress of the BCFZ to the arbitrary value $\sigma_2 = 450$ MPa. Again, as long as $a_2\sigma_2$ is of the order of 0.27 MPa, the choice of σ_2 has no influence on the fit to the evolution of the cumulated number of earthquakes.

[80] The viscosity of the ductile shear zone is not an explicit model parameter since only the factor $\nu w_3/\Delta h$ matters. According to equations (14), (9), and (2), we get $\nu w_3/\Delta h = G w_1 T_M/(w_1 + w_2)$, and hence $\nu w_3/\Delta h \simeq 4.9 \times 10^{12}$ Pa yr.

[81] **Acknowledgments.** M. Olcay, J. Campos, and J.-B. de Chabalier played a crucial role in this project by making the acquisition of continuous GPS data at station UAPF possible. We are grateful to Stéphane Mazzotti and Yehuda Bock for their thoughtful reviews and comments which helped to improve the manuscript. We thank T. Melbourne and F. Webb for providing us the time series of *Melbourne and Webb* [2002]. Discussions with H. Tavera, L. Audin, S. Bonvalot, D. Rémy, G. Hérail, and M. Chlieh have been helpful in the redaction of the manuscript. Figure 1 has been made using GMT of P. Wessel and W. H. F. Smith. Caltech Tectonic Observatory contribution 12.

References

Altamimi, Z., P. Sillard, and C. Boucher (2002), ITRF2000: A new release of the International Terrestrial Reference Frame for earth science applications, *J. Geophys. Res.*, *107*(B10), 2214, doi:10.1029/2001JB000561.

Avouac, J.-P. (2003), Mountain building, erosion, and the seismic cycle in the Nepal, Himalaya, *Adv. Geophys.*, *46*, doi:10.1016/S0065-2687(03)46001-9.

Bevis, M., E. C. Kendrick, R. Smalley Jr., T. Herring, J. Godoy, and F. Galban (1999), Crustal motion north and south of the Arica deflec-

tion: Comparing recent geodetic results from the central Andes, *Geochem. Geophys. Geosyst.*, *1*(1), doi:10.1029/1999GC000011.
Bilek, S. L., and L. J. Ruff (2002), Analysis of the 23 June 2001 M_w = 8.4 Peru underthrusting earthquake and its aftershocks, *Geophys. Res. Lett.*, *29*(20), 1960, doi:10.1029/2002GL015543.
Bills, B., D. Currey, and G. Marshall (1994), Viscosity estimates for the crust and upper mantle from patterns of lacustrine shoreline deformation in the Eastern Great Basin, *J. Geophys. Res.*, *99*, 22,059–22,086.
Blanpied, M. L., D. A. Lockner, and J. D. Byerlee (1995), Frictional slip of granite at hydrothermal conditions, *J. Geophys. Res.*, *100*, 13,045–13,064.
Bosl, W. J., and A. Nur (2002), Aftershocks and pore fluid diffusion following the 1992 Landers earthquake, *J. Geophys. Res.*, *107*(B12), 2366, doi:10.1029/2001JB000155.
Brown, L., R. Reilinger, S. Holdahl, and E. Balazs (1977), Postseismic crustal uplift near Anchorage, Alaska, *J. Geophys. Res.*, *82*, 3369–3378.
Buiter, S., R. Govers, and M. Wortel (2001), A modelling study of vertical surface displacements at convergent plate margins, *Geophys. J. Int.*, *147*, 415–427.
Burgmann, R., S. Ergintav, P. Segall, E. Hearn, S. McClusky, R. Reilinger, H. Woith, and J. Zschau (2002), Time-space variable afterslip on and deep below the Izmit earthquake rupture, *Bull. Seismol. Soc. Am.*, *92*, 126–137.
Chester, F. (1995), A rheologic model for wet crust applied to strike-slip faults, *J. Geophys. Res.*, *100*, 13,033–13,044.
Chlieh, M., J. de Chabalier, J. Ruegg, R. Armijo, R. Dmowska, J. Campos, and K. Feigl (2004), Crustal deformation and fault slip during the seismic slip in the north Chile subduction zone, from GPS and InSAR observations, *Geophys. J. Int.*, *157*, 1–17.
Cohen, S. (1998), On the rapid postseismic uplift along Turnagain Arm, Alaska following the 1964 Prince William Sound earthquake, *Geophys. Res. Lett.*, *25*, 1213–1215.
Cohen, S. (1999), Modeling of crustal deformation in seismic zones, *Adv. Geophys.*, *41*, 133–231.
DeMets, C., R. Gordon, D. Argus, and S. Stein (1990), Current plate motions, *Geophys. J. Int.*, *101*, 425–478.
Deng, J., K. Hudnut, M. Gurnis, and E. Hauksson (1999), Stress loading from viscous flow in the lower crust and triggering of aftershocks following the 1994 Northridge, California, earthquake, *Geophys. Res. Lett.*, *26*, 3209–3212.
Dieterich, J. H. (1979), Modeling of rock friction: 1. Experimental results and constitutive equations, *J. Geophys. Res.*, *84*, 2161–2168.
Dieterich, J. H. (1994), A constitutive law for rate of earthquake production and its application to earthquake clustering, *J. Geophys. Res.*, *99*, 2601–2618.
Dorbath, L., A. Cisternas, and C. Dorbath (1990), Quantitative assessment of great earthquakes in Peru, *Bull. Seismol. Soc. Am.*, *80*, 551–576.
Freymueller, J., S. Cohen, and H. Fletcher (2000), Spatial variations in present-day deformation, Kenai Peninsula, Alaska, and their implications, *J. Geophys. Res.*, *105*, 8079–8101.
Hearn, E., R. Burgmann, and R. Reilinger (2002), Dynamics of Izmit earthquake postseismic deformation and loading of the Duzce earthquake hypocenter, *Bull. Seismol. Soc. Am.*, *92*, 172–193.
Hindle, D., J. Kley, E. Klosko, S. Stein, T. Dixon, and E. Norabuena (2002), Consistency of geologic and geodetic displacements during Andean orogenesis, *Geophys. Res. Lett.*, *29*(8), 1188, doi:10.1029/2001GL013757.
Hsu, Y., N. Bechor, P. Segall, S. Yu, L. Kuo, and K. Ma (2002), Rapid afterslip following the 1999 Chi-Chi, Taiwan earthquake, *Geophys. Res. Lett.*, *29*(16), 1754, doi:10.1029/2002GL014967.
Hutton, W., D. DeMets, O. Sánchez, G. Suárez, and J. Stock (2001), Slip kinematics and dynamics during and after the 1995 October 9 M_w = 8.0 Colima-Jalisco earthquake, Mexico, from GPS geodetic constraints, *Geophys. J. Int.*, *146*, 637–658.
Khazaradze, G., K. Wang, J. Klotz, Y. Hu, and J. He (2002), Prolonged post-seismic deformation of the 1960 great Chile earthquake and implications for mantle rheology, *Geophys. Res. Lett.*, *29*(22), 2050, doi:10.1029/2002GL015986.
Kikuchi, M., and Y. Yamanaka (2001), Earthquake Information Center seismological note 105, Earthquake Inf. Cent., Earthquake Res. Inst., Univ. of Tokyo, Tokyo.
King, G. C. P., R. S. Stein, and J. Lin (1994), Static stress changes and the triggering of earthquakes, *Bull. Seismol. Soc. Am.*, *84*, 935–953.
King, R., and Y. Bock (1998), Documentation for the GAMIT GPS analysis software, version 9.7, Mass. Inst. of Technol., Cambridge.
Lamb, S. (2000), Active deformation in the Bolivian Andes, South America, *J. Geophys. Res.*, *105*, 25,627–25,654.
Marone, C. J., C. H. Scholz, and R. Bilham (1991), On the mechanics of earthquake afterslip, *J. Geophys. Res.*, *96*, 8441–8452.
Márquez-Azúa, B., C. DeMets, and T. Masterlark (2002), Strong interseismic coupling, fault afterslip, and viscoelastic flow before and after the Oct. 9, 1995 Colima-Jalisco earthquake: Continuous GPS measurements from Colima, Mexico, *Geophys. Res. Lett.*, *29*(8), 1281, doi:10.1029/2002GL014702.
Melbourne, T. I., and F. H. Webb (2002), Precursory transient slip during the 2001 M_w = 8.4 Peru earthquake sequence from continuous GPS, *Geophys. Res. Lett.*, *29*(21), 2032, doi:10.1029/2002GL015533.
Melbourne, T. I., F. H. Webb, J. M. Stock, and C. Reigber (2002), Rapid postseismic transients in subduction zones from continuous GPS, *J. Geophys. Res.*, *107*(B10), 2241, doi:10.1029/2001JB000555.
Miyazaki, S., P. Segall, J. Fukuda, and T. Kato (2004), Space time distribution of afterslip following the 2003 Tokachi-oki earthquake: Implications for variations in fault zone frictional properties, *Geophys. Res. Lett.*, *31*, L06623, doi:10.1029/2003GL019410.
Montési, L. G. J. (2004), Controls of shear zone rheology and tectonic loading on postseismic creep, *J. Geophys. Res.*, *109*, B10404, doi:10.1029/2003JB002925.
Nur, A., and J. Booker (1972), Aftershocks caused by pore fluid-flow, *Science*, *175*, 885–887.
Okada, Y. (1992), Internal deformation due to shear and tensile faults in a half-space, *Bull. Seismol. Soc. Am.*, *82*, 1018–1040.
Perfettini, H., and J.-P. Avouac (2004a), Postseismic relaxation driven by brittle creep: A possible mechanism to reconcile geodetic measurements and the decay rate of aftershocks, application to the Chi-Chi earthquake, Taiwan, *J. Geophys. Res.*, *109*, B02304, doi:10.1029/2003JB002488.
Perfettini, H., and J.-P. Avouac (2004b), Stress transfer and strain rate variations during the seismic cycle, *J. Geophys. Res.*, *109*, B06402, doi:10.1029/2003JB002917.
Pollitz, F., R. Burgmann, and P. Segall (1998), Joint estimation of afterslip rate and postseismic relaxation following the 1989 Loma Prieta earthquake, *J. Geophys. Res.*, *103*, 26,975–26,992.
Pollitz, F., G. Peltzer, and R. Burgmann (2000), Mobility of continental mantle: Evidence from postseismic geodetic observations following the 1992 Landers earthquake, *J. Geophys. Res.*, *105*, 8035–8054.
Rice, J. R. (1993), Spatio-temporal complexity of slip on a fault, *J. Geophys. Res.*, *98*, 9885–9907.
Rice, J. R., and A. L. Ruina (1983), Stability of steady frictional slipping, *J. Appl. Mech.*, *50*, 343–349.
Rice, J. R., and S. T. Tse (1986), Dynamic motion of a single degree of freedom system following a rate and state dependent friction law, *J. Geophys. Res.*, *91*, 521–530.
Ruegg, J.-C., M. Olcay, and D. Lazo (2001), Co-, post- and pre (?)-seismic displacements associated with the M_w 8.4 Southern Peru earthquake of 23 June 2001 from continuous GPS measurements, *Seismol. Res. Lett.*, *72*, 673–678.
Ruina, A. L. (1983), Slip instability and state variable friction laws, *J. Geophys. Res.*, *88*, 10,359–10,370.
Savage, J., and G. Plafker (1991), Tide gage measurements of uplift along the south coast of Alaska, *J. Geophys. Res.*, *96*, 4325–4335.
Scholz, C. H. (1990), *The Mechanics of Earthquakes and Faulting*. Cambridge Univ. Press, New York.
Scholz, C. H., and J. Campos (1995), On the mechanism of seismic decoupling and back arc spreading at subduction zones, *J. Geophys. Res.*, *100*, 22,103–22,116.
Segall, P., R. Burgmann, and M. Matthew (1995), Time-dependent triggered afterslip following the 1989 Loma Prieta earthquake, *J. Geophys. Res.*, *105*, 5615–5634.
Sella, G. F., T. H. Dixon, and A. Mao (2002), REVEL: A model for Recent plate velocities from space geodesy, *J. Geophys. Res.*, *107*(B4), 2081, doi:10.1029/2000JB000033.
Tavera, H., and E. Buforn (2001), Source mechanisms of earthquakes in Peru, *J. Seismol.*, *5*, 519–539.
Tavera, H., E. Buforn, I. Bernal, Y. Antayhua, and L. Vilacapoma (2002), The Arequipa (Peru) earthquake of June 23, 2001, *J. Seismol.*, *6*, 279–283.
Wang, K., J. He, H. Dragert, and T. S. James (2001), Three-dimensional viscoelastic interseismic deformation model for the Cascadia subduction zone, *Earth Planets Space*, *53*, 295–306.
Zumberge, J., R. Liu, and R. Neilan (1995), *International GPS Service for Geodynamics*, 329 pp., IGS Cent. Bur., Pasadena, Calif., Sept.

J.-P. Avouac, Geological and Planetary Sciences, California Institute of Technology, Mail code 100-23, Pasadena, CA 91125, USA. (avouac@gps.caltech.edu)

H. Perfettini, Institut de Recherche pour le Développement/Laboratoire des Mécanismes de Transferts en Géologie, Observatoire Midi-Pyrénées, 14 avenue Edouard Belin, F-31400 Toulouse, France. (perfetti@lmtg.obs-mip.fr)

J.-C. Ruegg, Institut de Physique du Globe, 4 place Jussieu, F-75252 Paris cedex 05, France. (ruegg@ipgp.jussieu.fr)